

Comparison of Mixing Characteristics for Several Fuel Injectors on an Open Plate and in a Ducted Flowpath Configuration at Hypervelocity Flow Conditions

Tomasz G. Drozda,[†] Rajiv R. Shenoy,[‡] Bradley J. Passe,[§] Robert A. Baurle,[†]
and J. Philip Drummond[¶]

NASA Langley Research Center, Hampton, VA 23681

ABSTRACT

In order to reduce the cost and complexity associated with fuel injection and mixing experiments for high-speed flows, and to further enable optical access to the test section for nonintrusive diagnostics, the Enhanced Injection and Mixing Project (EIMP) utilizes an open flat plate configuration to characterize inert mixing properties of various fuel injectors for hypervelocity applications. The experiments also utilize reduced total temperature conditions to alleviate the need for hardware cooling. The use of “cold” flows and nonreacting mixtures for mixing experiments is not new, and has been extensively utilized as a screening technique for scramjet fuel injectors. The impact of reduced facility-air total temperature, and the use of inert fuel simulants, such as helium, on the mixing character of the flow has been assessed in previous numerical studies by the authors. Mixing performance was characterized for three different injectors: a strut, a ramp, and a flushwall. The present study focuses on the impact of using an open plate to approximate mixing in the duct. Toward this end, Reynolds-averaged simulations (RAS) were performed for the three fuel injectors in an open plate configuration and in a duct. The mixing parameters of interest, such as mixing efficiency and total pressure recovery, are then computed and compared for the two configurations. In addition to mixing efficiency and total pressure recovery, the combustion efficiency and thrust potential are also computed for the reacting simulations.

Statement A: Approved for public release; distribution is unlimited.

[†]Research Aerospace Engineer, Hypersonic Airbreathing Propulsion Branch

[‡]Research Engineer, Analytical Mechanics Associates, Inc.

[§]Research Engineer, (formerly) Analytical Mechanics Associates, Inc.

[¶]Distinguished Research Associate, Hypersonic Airbreathing Propulsion Branch

INTRODUCTION

Fuel injector design, fuel-air mixing, and efficient combustion and flameholding remain some of the key fluid dynamic challenges in scramjet flowpath design. Attempts to improve fuel injection by enhancing the fuel-air mixing, while simultaneously reducing total pressure losses have received a great deal of attention over the years.¹ Although some total pressure loss is thermodynamically unavoidable and occurs as a result of the desired effect of molecular mixing of the fuel and air, any losses beyond this minimum amount reduce the thrust potential of the engine and should be minimized.

The Enhanced Injection and Mixing Project (EIMP), being executed at the NASA Langley Research Center, represents an effort to achieve more rapid mixing at high speeds.² The EIMP aims to investigate scramjet fuel injection and mixing physics, improve the understanding of underlying physical processes, and develop enhancement strategies relevant to flight Mach numbers greater than eight. In the experiments, which are underway in the Arc-Heated Scramjet Test Facility (AHSTF), various fuel injection devices are being tested on an open flat plate located downstream of a Mach 6 facility nozzle, which simulates the combustor entrance of a flight vehicle traveling at a Mach number of about 14 to 16. An open flat plate geometry was chosen, as opposed to a closed duct, in order to facilitate optical access for nonintrusive diagnostics and to simplify the experiment. Furthermore, the tests are conducted at reduced total temperature and with an inert fuel simulant (helium) to allow for uncooled test hardware, thereby further reducing the complexity and cost of the experiment. The impact of both reduced total temperature and the use of inert fuel on the mixing character of the flow has been previously assessed computationally.³ The mixing performance of three baseline fuel injectors: a strut, a ramp and a flushwall, under the experimental conditions, has also been characterized computationally.⁴ In the present study, computational simulations continue to be utilized, with the goal of assessing the impact that the open plate configuration and injector arrangement have on the mixing flowfield, by performing simulations for three baseline fuel injectors on an open plate and in a closed duct, both at notional flight conditions. The mixing parameters of interest, including mixing and combustion efficiencies, total pressure recovery, and the thrust potential, are then computed and compared between the two configurations.

INJECTOR GEOMETRIES, CONFIGURATIONS, AND SIMULATED FLOW CONDITIONS

Three types of injectors were investigated in the current study. These are a strut, a ramp, and a high-aspect ratio rectangular flushwall injector. The strut and ramp were previously studied by Baurle et al.⁵ under “cold” flow conditions at a combustor entrance Mach number of 4.5. The flushwall injector geometry is based on the multiobjective optimization work of Ogawa.⁶ Isometric views and dimensional details of the strut, ramp, and flushwall injectors are shown in Figs. 1-3, where x , y , and z denote the streamwise (or downstream), vertical (or wall normal), and cross-stream directions, respectively.

The strut injector is a slender swept strut protruding into the flow. Strut injectors have several advantages in hypervelocity flow applications. First, they can be designed to place the fuel where it is needed, thereby alleviating the need to consider fuel penetration issues and focusing only on the injector spacing. Second, the injector ports on a strut are typically aligned parallel to the flow, which allows the injected fuel streams to augment the thrust of the engine. The potential disadvantages of a strut injector are: the structural integrity and cooling requirements needed for its slender body, the drag (both viscous and pressure) that it induces on the flow by the obstruction it generates, and the total pressure loss incurred by the oblique shocks that emanate from its leading edge. These shock waves introduce mixing enhancement via the effect of baroclinic torque as they pass through the variable density interfaces of fuel-air mixing plumes and induce localized vorticity right at the interface of fuel and air. However, these positive effects compete with the added total pressure losses. In the current simulations, the struts are placed 0.9 inches apart in the z -direction. This spacing is the same as that found in the previous work of Baurle et al.⁵ Each strut injector has four fuel injector ports. Each injector port has a throat diameter of 0.083 inches followed by a

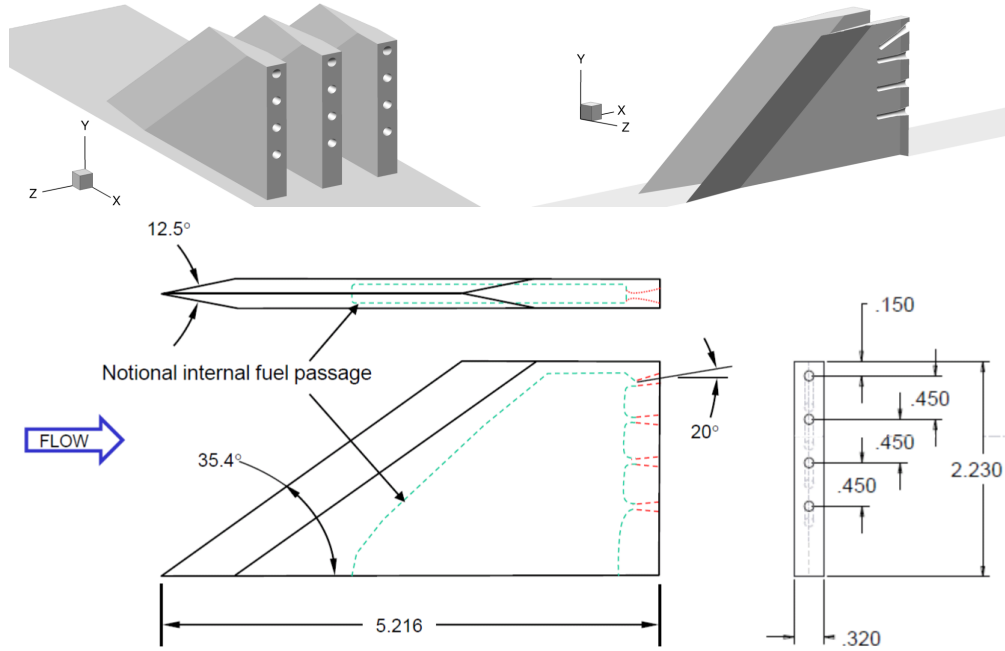


Figure 1. Isometric views and dimensional details of the baseline strut injector (dimensions are in inches).

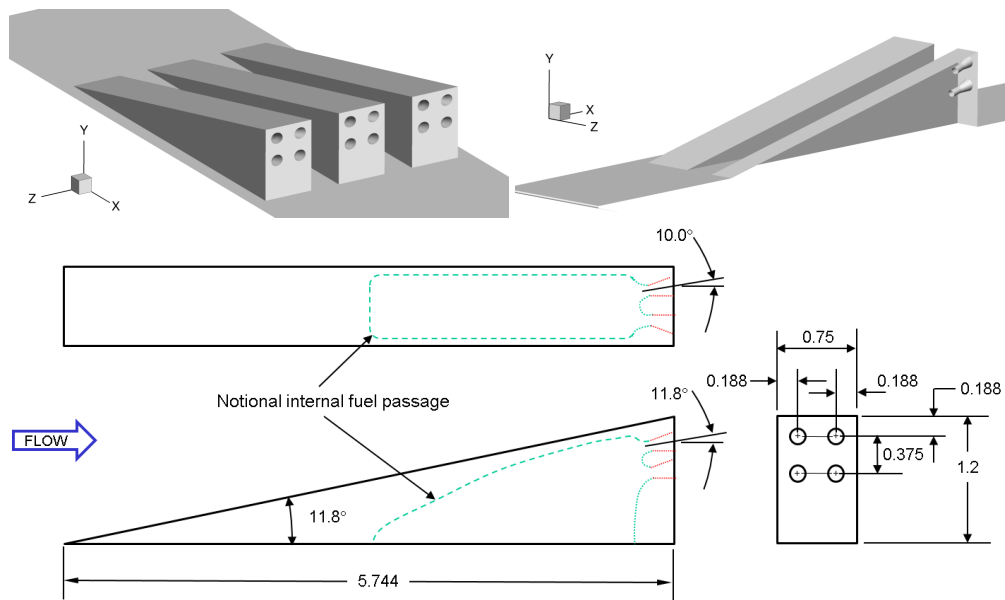


Figure 2. Isometric views and dimensional details of the baseline ramp injector (dimensions are in inches).

conical expansion area with a half-angle of 6 degrees that expands hydrogen, which is used as the fuel in the present study, to an exit Mach number of approximately 2.6.

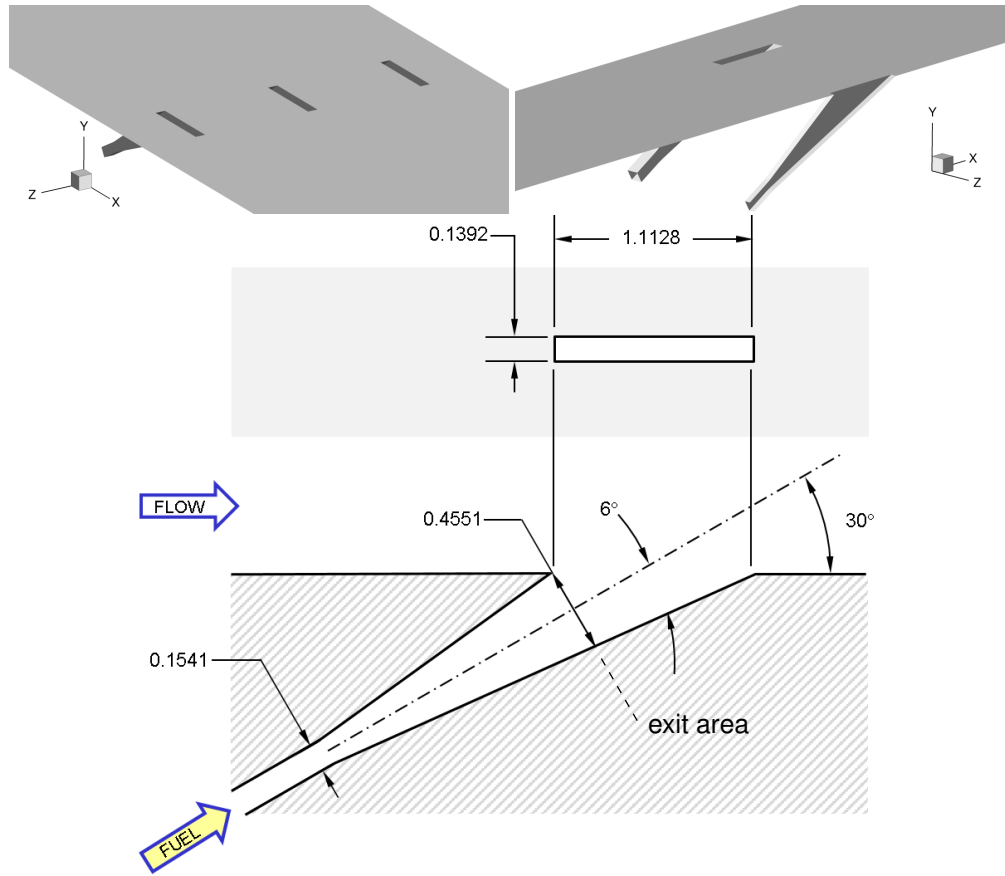


Figure 3. Isometric views and dimensional details of the baseline flushwall injector (dimensions are in inches).

The ramp injector generates a counter-rotating vortex pair (CVP) with one vortex on each side of the unswept ramp as the flow passes over the ramp and through the gaps between the ramps. The CVP convects the injected fuel upward, toward the core of the flow, and fills the combustor cross-section area. In addition to inducing the upward entrainment, the CVP stretches the fuel-air interface thereby increasing the surface area over which the molecular viscosity can act to mix the fuel and air. Because the strength of the CVP depends on both the geometry of the ramp, and the incoming air flow conditions, designing an injector that robustly fills the combustor cross-section area across a range of flight conditions is more challenging for a ramp than a strut. As with the strut, the ports of the ramp injector are also nearly aligned parallel to the flow and allow for injected fuel streams to augment the thrust of the engine. In the current configuration, the ramp ports are angled slightly up and to the side to aid in directing the fuel streams toward the CVP. The ramp injector also generates an oblique shock due to its inclined surface. As in the case for the shock waves generated by the strut injector leading edge, the ramp shock also induces total pressure losses. Because the ramp induces only a single oblique shock, the total pressure losses are expected to be smaller than those for the struts, but the potential for mixing enhancement via the baroclinic torque is also reduced. In the current simulations, ramp spacings of 1.2 and 2.4 inches were investigated. The latter spacing is also the same as that found between the interdigitated ramp configuration of Baurle et al.⁵ Each injector port has a throat diameter of 0.108 inches followed by a conical expansion area with a half-angle of 10 degrees that has the same expansion area ratio as the strut and expands hydrogen to an exit Mach number of about 2.6.

Table 1. Flight freestream conditions in the current simulations.

Alt. (km)	Mach No.	Q (kPa)	P (kPa)	T (K)	T_0^\dagger (K)	P_0^\dagger (MPa)
36.6	14.94	71.82	0.4603	249.2	8748.4	1294.7

[†]Value based on frozen composition of air

Unlike the strut and ramp, the flushwall injector does not introduce a physical blockage into the flow. Instead, a number of flow features form around the injection site that interact to produce a similar effect. The bow shock that forms upstream of the injection plume creates total pressure losses and aerodynamic blockage by forcing the air to flow around the fuel plume. As in the case for the ramp injector, the fuel plume entering the high-speed crossflow generates a CVP, which becomes the main mechanism for stirring the fuel into the air. However, unlike a fuel placement device such as a strut, the extent to which the fuel penetrates into the airflow is governed by fluidic considerations.^{1,7-9} The jet penetration has been shown to be primarily proportional to the ratio of the orthogonal components of the dynamic pressure (or momentum flux) of the main air and the fuel jet, and is further enhanced by matching the static pressure at the exit of the fuel injector to the static pressure of the air just upstream of the fuel plume and downstream of the bow shock. The injector port has a rectangular cross-section, with an aspect ratio of 8 at the injector exit plane, with the longer dimension aligned with the streamwise direction. The injector is also inclined at 30 degrees to the wall. Injector spacings of 0.852 and 1.704 inches (in the z-direction) were investigated. The latter spacing, obtained from optimization,⁶ corresponds to about 6 times the diameter of a circular injector with an equivalent area, and about 1.5 times the longer dimension of the current injector, allowing for an air-gap between the adjacent injectors sufficiently large to accommodate the expected axis-switching of the fuel plume.⁶ The flushwall injector also contains an expansion section with a 6 degree half-angle. With the injector exit as denoted in Fig. 3, the expansion area ratio matches that of the conical fuel port of both the strut and the ramp. The exit area also matches the total exit area of the 4 fuel ports of the strut.

In previous studies, the performance of the three injectors was compared at experimental ground conditions,^{3,4} as well as nominal flight conditions.³ It was found that the mixing efficiency obtained from the numerical simulations of the ground experiments using helium matched well with that found at the flight conditions using hydrogen.³ However, in all the previous studies, only the experimental injector configurations were investigated. These configurations consisted of a row of injectors mounted on an open flat plate positioned downstream of a Mach 6 facility nozzle. The facility nozzle flow simulates a nondistorted combustor entrance flow (i.e., post inlet compression) of a flight vehicle traveling at a Mach number of about 14 to 16. The flat plate is 28.87 inches long tip-to-tail with the fuel injection plane located 8.87 inches downstream from the leading edge of the plate. Further details about the experimental setup and the EIMP are presented in Cabell et al.²

In the current work, the impact that the confinement of the injector configuration in a duct has on the mixing characteristics and performance as compared to experimentation on an open flat plate is evaluated. Because previous numerical simulation results indicated good agreement between the mixing characteristics of helium on the ground and hydrogen in flight,³ and the ducted flowpath is not available for the ground experiments, the current work focuses on the mixing characteristics of hydrogen under nominal flight conditions. These conditions are obtained by proposing a hypothetical inlet process that compresses the freestream air to half an atmosphere and a Mach number equal to the approach Mach number in the ground tests (i.e., about 6) at the combustor entrance. The inlet compression is assumed to have a 95% isentropic efficiency and 99% adiabatic efficiency.¹⁰ The kinetic energy efficiency of this notional inlet is about 98%. Further assuming a nominal vehicle flight path along a constant dynamic pressure trajectory of 1500 psf, and using the standard atmosphere tables,¹¹ gives the nominal flight conditions, which in this case correspond to about Mach 15 flight at an altitude of about 120 kft. The freestream conditions obtained by following the above outlined approach, and used in the current simulations, are shown in Table 1.

The injector configurations on the open flat plate are the same as those found in authors' previous work.^{3,4} In those simulations, the computational domain extended 6 inches vertically, which approximated the height

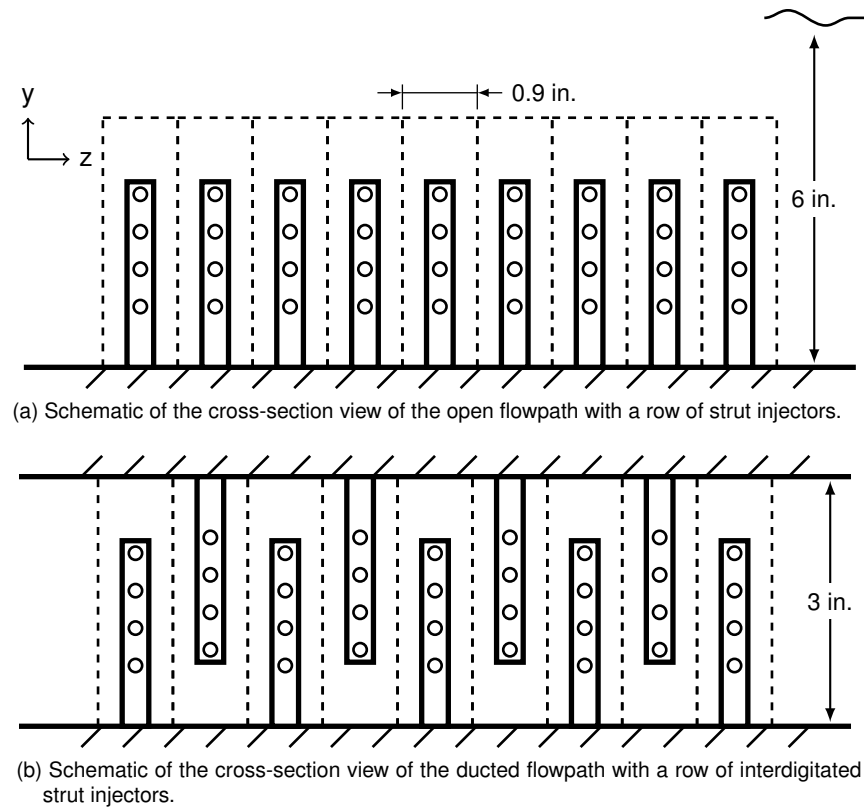


Figure 4. Schematic of the cross-section view of the strut injectors installed on the open plate (a), and in the ducted configuration (b). The dashed lines denote the intended fueling area for each injector.

of the EIMP facility nozzle core flow.¹² The ducted configurations are obtained by mirroring the flat plate configuration about the x-z plane at a distance of 1.5 inches above the flat plate, resulting in a 3 inch high duct. Furthermore, removing every other injector in an alternating pattern from both flat plates produces an interdigitated injector configuration. This procedure produces the same injector configurations as those studied previously by Baurle et al.⁵ The schematic view of the flow cross section for the three different injectors installed on the open flat plate and in the ducted configuration are shown in Figs. 4-6.

The intended fueling area (IFA) is defined as the portion of the cross-sectional area of the duct that each injector is expected to fuel independently of others. For example, a combustor cross-section area fueled with slender struts, which nearly span the full height of the duct, will likely require such devices to be spaced more narrowly than a similar combustor fueled with large vortex generating ramps. Therefore, the IFA will be narrower for struts than for the ramps. The IFAs for the strut and ramp are obtained from Baurle et al.,⁵ who already investigated these injectors in a 3 inch high ducted scramjet combustor configuration, albeit at different flow conditions. Since the flushwall injector was not designed to place the fuel far from the wall, as does the strut, and relies on a CVP to stir the fuel, as does the ramp, the IFA height for the flushwall injector is the same as that for the ramp with the width obtained equal to 1.704 inches (i.e., optimized injector spacing). The effect of the injector spacing was also investigated for the open flat plate configurations for the ramp and flushwall injectors. For those cases, the injector spacing, and the corresponding IFAs, have been reduced by half as seen in Figs. 5(a), and 6(a). The narrow placement of the ramps or flushwall injectors reduces their vortex-generating capability in exchange for a more distributed placement of fuel, higher flow blockage, and body-induced drag.

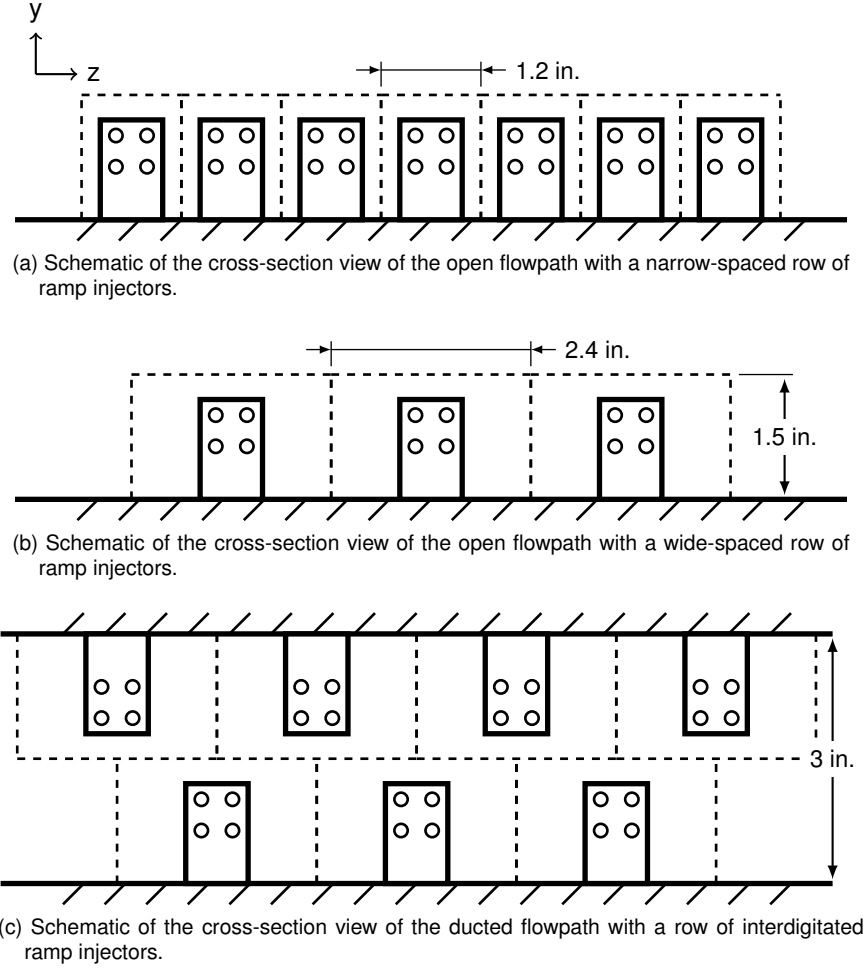


Figure 5. Schematic of the cross-section view of the narrow- and wide-spaced ramp injectors installed on the open plate (a,b), and in the ducted configuration (c). The dash lines denote the intended fueling area for each injector.

The flowpath entrance flow conditions correspond to a static pressure and static temperature of 50.66 kPa and 1297.8 K, respectively, with a Mach number of 6.36. A thermally perfect mixture of 21% oxygen (O_2) and 79% nitrogen (N_2) by volume was used for the air. The fuel mass flow rate of hydrogen for each injector was computed by assuming an equivalence ratio (ER) of 0.75 over the IFA. The details of all the flow parameters used in the current simulations are shown in Table 2, where the properties for air and fuel are presented. The subscripts f and a denote fuel and airflow streams, respectively. In addition to the quantities needed for the simulations, quantities that have been found to be relevant to injection and mixing in canonical problems^{13–15} are also shown; these are, the unit Reynolds numbers for the air and fuel streams, Re' , velocity difference parameter, ΔU , the convective Mach number, M_c , and the ratios of the static density, ρ_f / ρ_a , static pressure, p_f / p_a , and dynamic pressure, J between the fuel and air stream. All values are computed based on the flowpath entrance flow conditions for the air and the expanded flow conditions at the exit of the injector ports for the fuel. The two leading order parameters that impact small scale mixing, i.e., the velocity difference parameter and the convective Mach number, are the same for all cases, allowing the focus of the present study to be on the impact of large-scale inviscid flow features on mixing.

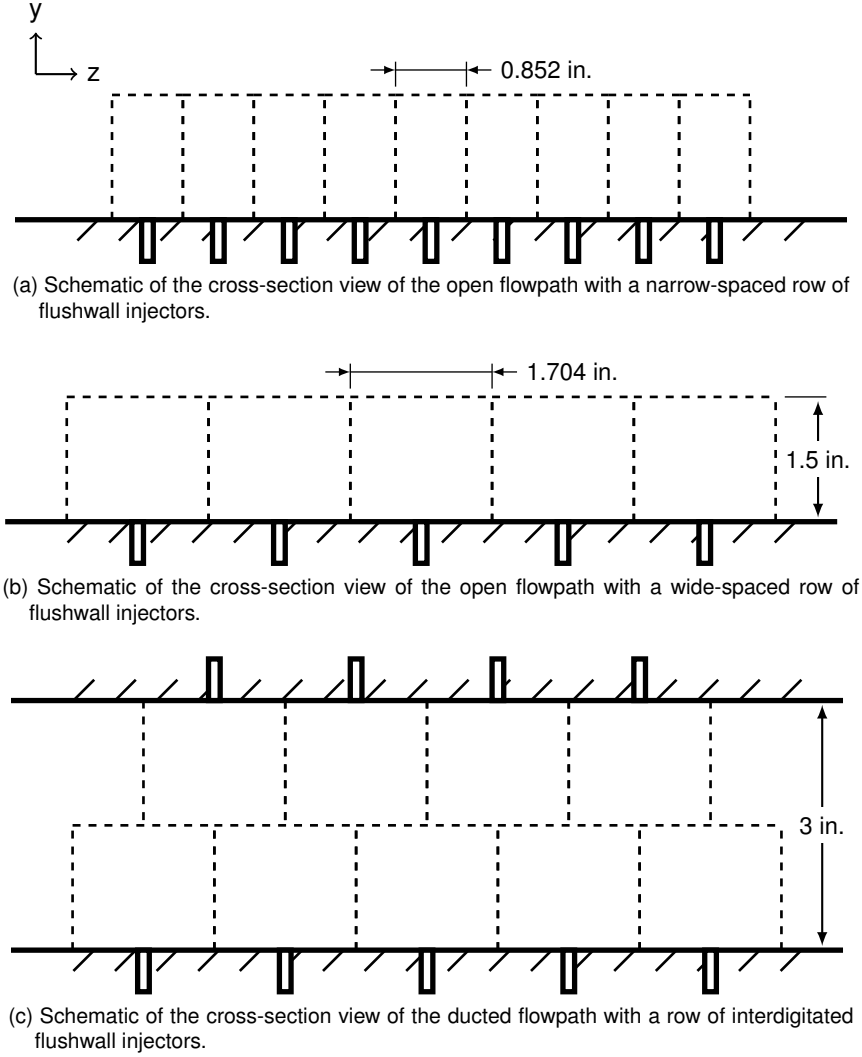


Figure 6. Schematic of the cross-section view of the narrow- and wide-spaced flushwall injectors installed on the open plate (a,b), and in the ducted configuration (c). The dash lines denote the intended fueling area for each injector.

METRICS OF INTEREST

A number of different metrics for mixing and combustion efficiency, thermodynamic losses, and thrust performance exist with a rigorous analysis proposed by Riggins et al.¹⁶ For the current study, the following were chosen: mass-flux-weighted Mach number, the total pressure recovery, mixing efficiency based on stoichiometric proportions of fuel and air, thrust potential, and combustion efficiency based on fuel depletion. The mass-flux-weighted Mach number is obtained from:

$$\overline{M} = \frac{\int M \rho u dA}{\int \rho u dA}, \quad (1)$$

where M is the Mach number, ρ is the static density, u and dA are the streamwise velocity magnitude and the incremental area projected in the streamwise direction, respectively, and the overbar denotes a one-dimensional property. This mass-flux-weighted Mach number is useful in revealing the global behavior of the flow, and the extent of margin with respect to choked flow conditions. The total mass-flux-weighted

Table 2. Global parameters of interest for the strut, ramp, and flushwall injector configurations. The last set of rows contains ratios of interest between the fuel (hydrogen) and air streams, where the subscripts f and a denote fuel and air streams, respectively.

	Air [†]	Fuel				
Property		Strut	Ramp		Flushwall	
Area WxH (in^2) [‡]		0.9 x 3.0 [§]	2.4 x 1.5	1.2 [¶] x 1.5	1.704 x 1.5	0.852 [¶] x 1.5
Mach	6.356	2.608	2.594	2.594	2.608	2.608
P_o (MPa)	295.4	5.384	4.240	2.120	5.097	2.548
T_o (K)	8672.8	1172.6	1172.6	1172.6	1172.6	1172.6
P (kPa)	50.66	263.9	212.6	106.3	249.9	124.9
T (K)	1297.8	504.5	507.7	507.7	504.5	504.5
u (m/s)	4461.1	4447.0	4436.4	4436.4	4447.0	4447.0
Re'/in x10e3	302.7	1133.6	901.3	450.7	1073.1	536.6
\dot{m}_a (kg/s) x10e-3		1052.5	1403.7	701.8	996.3	498.2
\dot{m}_f (kg/s) x10e-3		23.05	30.74	15.37	21.82	10.91
ER**		0.75	0.75	0.75	0.75	0.75
ΔU ^{††}		-0.0016	-0.0029	-0.0028	-0.0016	-0.0016
M_c ^{‡‡}		0.0059	0.0103	0.0103	0.0059	0.0059
ρ_f / ρ_a		0.9364	0.7494	0.3747	0.8865	0.4432
P_f / P_a		5.2098	4.1963	2.0982	4.9319	2.4660
J ^{§§}		0.9305	0.7412	0.3706	0.8808	0.4404

[†]21% O₂, 79% N₂

[‡]Intended fueling area for the injector

[§]Nominal height of a duct

[¶]Narrow injector spacing

^{||}Value based on the frozen composition of air.

^{**}ER with respect to the IFA

^{††}Velocity difference parameter, $\Delta U = (u_f - u_a)/(u_f + u_a)$

^{‡‡}Convective Mach number, $M_c = |u_f - u_a|/(c_f + c_a)$, c denotes the speed of sound.

^{§§}Dynamic pressure ratio, $J = (\rho_f u_f^2)/(\rho_a u_a^2) = (\dot{m}_f' u_f)/(\dot{m}_a' u_a)$.

pressure recovery is defined as:

$$\overline{P}_o^{rec} = \frac{1}{P_{o_i}} \frac{\int P_o \rho u dA}{\int \rho u dA}, \quad (2)$$

where P_o , and P_{o_i} are the local and reference (e.g., free stream, flowpath entrance) values of the total pressure, respectively. This parameter is proportional to the difference between sensible entropies computed at the total and static values of the temperature, and therefore, gives a measure of the thermodynamic losses. For mixing simulations, the total pressure recovery quantifies the losses due to the drag on the injector bodies and the surface of the flat plate, the mechanical stirring induced by injector bodies (especially the ramp), the turbulence, and the molecular mixing. For reacting simulations, the total pressure recovery is further reduced by the entropy increases due to the chemical reactions, therefore, the values of the total pressure recovery obtained from the mixing simulations can be thought of as the maximum achievable for a given injector. Because chemical reactions reduce the total pressure recovery, which can be interpreted as a loss, yet energize the flow via heat release, which can be expanded into thrust, there is a need for another metric which can more objectively quantify the potential performance of the flowpath. The most direct metric that can achieve this is the thrust potential. This metric is obtained by expanding one-dimensional values of the flow variables at each streamwise location through an ideal (isentropic) thrust nozzle. In the current work, this (thermodynamic) process is evaluated until the flow reaches the flowpath entrance value of the static pressure. The thrust potential is then computed from (see Appendix A for details):

$$\overline{TP} = \dot{m}_e u_e + (p_e - p_i) A_e - \dot{m}_i u_i \quad (3)$$

where TP is the thrust potential, \dot{m} , u , p , A , are the mass flow rate, velocity, static pressure, and the area, with subscripts e and i denoting conditions at the thrust nozzle exit plane, and the flowpath entrance (inflow), respectively. Since the flow expands to the inflow stream static pressure, the second term in the above equation is identically zero. Furthermore, since $\dot{m}_i u_i$ is a constant offset, it is lumped with the value of the thrust potential. This metric represents an ideal potential net thrust (not stream thrust) that could be obtained when a flowpath of interest is truncated at a given streamwise location and coupled at that location to an ideal thrust nozzle. However, the flow in the thrust nozzle is assumed to be chemically “frozen” starting at the point of expansion, and therefore, this metric does not account for any mixing (losses) and reaction (thrust increases) during the expansion process, which could either further decrease or increase the thrust. Furthermore, because the flowpath entrance static pressure, not the static pressure upstream of the hypothetical inlet, is used in the expansion process, the current metric only accounts for the portion of a potential thrust. Nevertheless, the values still reveal whether the losses introduced by the current flowpath and injector system can be overcome by the streamwise injection and chemical reaction processes. All of the losses in the value of the total pressure previously discussed still appear as a decrease in the value of the thrust potential, however, the chemical reactions, which energize the flow, could increase the value of the thrust potential. The specific thrust potential, i.e., the thrust potential divided by the mass flow rate of inflow air, can also be computed. The mass flow rate normalization is useful for comparing flowpaths of different sizes or containing fuel injectors designed to fuel different areas per injector.

The mixing efficiency is defined in this work following Mao et al.:⁸

$$\eta_m = \frac{\int \alpha_R \rho u dA}{\int \alpha \rho u dA} \quad (4)$$

where the integration is over a single streamwise, constant cross-stream plane (x-plane) of interest, and α is the fuel or oxidizer mass fraction depending on whether the global ER is less than or greater than 1, respectively. The overbar denoting a one-dimensional property of the mixing efficiency is omitted because these quantities are only defined in the integrated sense. The quantity α_R is defined as the amount of fuel or oxidizer that would react if complete reaction took place without further mixing, i.e.,

$$\alpha_R = \begin{cases} \alpha, & \alpha \leq \alpha_{st} \\ \frac{\alpha_{st}}{1-\alpha_{st}}(1-\alpha), & \alpha > \alpha_{st} \end{cases} \quad (5)$$

where α_{st} is the stoichiometric value of fuel or oxidizer mass fraction. For cases with overall ER of one, either fuel or oxidizer can be used in place of α . However, choosing the fuel has a minor benefit of clarifying somewhat the meaning of Eq. (5), which becomes

$$\alpha_R = \begin{cases} Y_f, & Y_f \leq Y_{f,st} \\ FAR_{st} Y_a, & Y_f > Y_{f,st} \end{cases} \quad (6)$$

where Y denotes mass fraction, and subscripts f and a denote fuel and air streams, respectively. The quantity FAR_{st} denotes the stoichiometric value of the fuel-to-air ratio and equals to 0.0293 for hydrogen-air mixtures. It is clear from the above equation that if the local value of the mass fraction of fuel is less than its stoichiometric value, then that amount is “counted” as fully mixed because there is a sufficient amount of air to potentially deplete all of the fuel if reactions were allowed. However, when the local value of the fuel mass fraction is greater than its stoichiometric value, then the only part that could react is that which is in stoichiometric proportion to the local value of the mass fraction of the air. Therefore, only that portion is counted as being mixed in Eq. (4). The stoichiometric value of the hydrogen mass fraction is 0.0285. The mixing efficiency formula of Mao et al.⁸ can also be used to analyze mixing in the reacting simulations, however, since fuel and oxidizer are consumed to make combustion products, care must be taken to use the elemental mass fractions of either fuel or oxidizer (i.e., mass fractions of all elements that originate in either fuel or oxidizer streams).

The combustion efficiency quantifies how completely a given flowpath is able to process a mixture of fuel and air into combustion products, thereby enabling heat release into the flow. There exists a number of

combustion efficiency definitions that include combinations of the total temperature, the enthalpy or enthalpy of formation as a function of the local equilibrium composition, and the fuel/oxidizer depletion or combustion product formation.¹⁷ In this work, the simplest definition based on the fuel mass fraction depletion is used, i.e.,

$$\eta_c = 1 - \frac{\dot{m}_f}{\dot{m}_{f,tot}} \quad (7)$$

where \dot{m}_f and $\dot{m}_{f,tot}$ are the integrated mass flow rates of fuel at a streamwise location of interest and the total injected fuel flow rate, respectively. For mixing-only simulations, the above quantity is identically zero, whereas for reacting simulations, its value increases monotonically to one when all of the fuel has been depleted. For fuel-rich simulations, the formulation based on the oxidizer mass fraction depletion would be appropriate.

When comparing the above quantities between the open plate and ducted configurations, care must be taken to properly account for different amounts of air mass flowing through the duct and over the open plate. For quantities such as mixing and combustion efficiencies, the comparisons are direct and no corrections are needed because these quantities are zero-valued outside of the injector IFAs, and both are further normalized with respect to the quantities that are only nonzero in the IFAs. However, for other quantities, the one-dimensional values obtained from the open flat plate simulations with a 6 inch high domain will be skewed (or weighted) toward the core flow conditions and must therefore be corrected to obtain meaningful comparisons with the same quantities obtained from the ducted simulations. The simplest approach is to truncate the open plate simulation domain to the duct height before performing one-dimensional analysis. However, it should be noted that for this correction approach, mass flow can freely move in and out of the truncated domain, which can impact the one-dimensional analysis results in uncontrolled ways. To avoid this issue, a correction based on ratios of the areas through the open and ducted flowpaths is developed. The assumptions invoked when deriving the corrections used in the present work are discussed in Appendix B. For a generic, mass-flux-weighted, one-dimensional, quantity $\bar{\phi}$ obtained from the open flat plate simulations, the corrected quantity equivalent to that in the duct is:

$$\hat{\phi} \approx \bar{\phi} \frac{A}{A_1} - \phi_\infty \frac{A - A_1}{A_1}, \quad (8)$$

where $\bar{\phi}$ is the one-dimensional quantity obtained from the open plate simulations, ϕ_∞ is the flowpath entrance value of the same quantity, A is the total area over the flat plate, A_1 is the area of interest, e.g., duct or IFA, and the “hat” denotes resulting corrected one-dimensional quantity. For the strut injectors the IFA is the same as the area of the duct. However, for the ramp and flushwall injectors, the IFA is half the height of the duct (see Figs. 5 and 6). For those injectors, applying the correction to their respective IFAs has the potential to at least partially account for the losses induced by the top plate of the duct because this plate is symmetric about the height of the IFA (half-height of the duct). Because the total pressure recovery is the mass-flux-weighted total pressure normalized by the freestream total pressure, the correction for this parameter takes on the form:

$$\hat{P}_o^{rec} \approx \bar{P}_o^{rec} \frac{A}{A_1} - \frac{A - A_1}{A_1}. \quad (9)$$

Finally, for the specific thrust potential:

$$\frac{\widehat{TP}}{\dot{m}} \approx \frac{\overline{TP}}{\dot{m}} - \frac{TP_\infty}{\dot{m}} \frac{A - A_1}{A}, \quad (10)$$

where \dot{m} is the mass flow rate through the area over the flat plate. Unless otherwise noted, all of the one-dimensional quantities for the open plate configurations presented in the current work have been corrected to the duct area using the area ratio approach discussed above. Therefore, both the overbar (for the ducted cases) and the “hat” notations to denote the one-dimensional values in the results section are omitted.

NUMERICAL CONSIDERATIONS

The numerical simulations were performed using the Viscous Upwind aLgorithm for Complex flow ANalysis (VULCAN-CFD) code.¹⁸ VULCAN-CFD is a multiblock, cell-centered, finite-volume solver widely used for high-speed flow simulations. For this work, Reynolds-averaged simulations (RAS) were performed. The advective terms were computed using the Monotone Upstream-Centered Scheme for Conservation Laws (MUSCL) scheme¹⁹ with the Low-Dissipation Flux-Split Scheme (LDFSS) of Edwards.²⁰ The thermodynamic properties of the mixture components were computed using the curve fits of McBride et al.²¹ The governing equations were integrated using an implicit diagonalized approximate factorization (DAF) method.²² The current work used the Menter Baseline two-equation turbulent physics model.²³ The Reynolds heat and species mass fluxes were modeled using a gradient diffusion model with turbulent Prandtl and Schmidt numbers of 0.9 and 0.5, respectively. Wilcox wall matching functions²⁴ were also used, however, their implementation in VULCAN-CFD includes a modification that allows the simulations to recover the integrate-to-the-wall behavior as the value of normalized wall-distance, y^+ , approaches one. All simulations were converged until the total integrated mass flow rate and the total integrated heat flux on the walls remained constant to at least 4 decimal points. This typically occurred when the value of the L_2 -norm of the steady-state equation-set residual decreased by about 4–5 orders of magnitude. To conserve the available computational resources, all the simulations were split into elliptic and space-marching regions. The elliptic region contained the inflow of the domain, the injector bodies, and up to 6.5 inches downstream of the injection plane. The computational cell count was about equal in both regions, but the computational cost associated with solving the space-marching regions was about an order of magnitude lower than that for the elliptic region. A single, fully elliptic simulation on a coarse grid confirmed that this approach indeed did not have a significant impact on any of the flow features nor the integrated values of the metrics of interest discussed in the previous section.

For the simulations on the open flat plate, three grids: coarse, medium, and fine, each progressively finer by a factor of 2 in each of the three dimensions, were used. The grid resolutions for the open plate simulations are summarized for the three injector types in Table 3. For the strut injector, a single full strut injector was included in the computational domain. Although this approach doubled the required domain size, it helped to alleviate some of the grid skewness issues at the top of the strut and near the leading edge of the strut. For the ramp injector case, only half of a ramp injector was included in the computational domain, taking advantage of all available symmetries to reduce the grid size requirement. The flushwall injector simulations also utilized all available symmetries. For the ramp and flushwall injectors, grids described in Table 3 were constructed for the narrowly spaced injectors (see Table 2). Consequently, for the wide-spaced configurations, the total computational node counts increased proportionally with the computational domain width.

All grids were generated with GridPro in the vicinity of the injector bodies and the leading edge of the flat plate, and further combined with Pointwise-generated h-blocks to complete the computational definition of the geometry. For all injectors, the inflow and outflow planes are placed 9 inches upstream and 25 inches downstream of the fuel injection plane, which is located at $x = 0$. Since both the inflow and the outflow consist of supersonic flow, the mixture composition, static values of the temperature and pressure, and the Mach number are specified at the inflow, and all flow variables are extrapolated at the outflow. Slip wall boundary conditions are used for the upper boundary of the open flat plate flow domain. This upper

Table 3. Number of computational nodes used in the current simulations of the narrowly-spaced injectors in the open plate configuration.

	Strut	Ramp	Flushwall
Coarse	4,921,682	4,057,382	4,356,936
Medium	39,373,456	32,459,056	34,855,488
Fine	314,987,648	259,672,448	278,843,904

boundary is 6 inches away from the flat plate, which approximates the height of the facility nozzle core flow. Because the simulation domain effectively includes an infinite row of injectors in the cross-stream, the current simulations model the experiment as an infinitely wide duct. In this model duct, the flow blockage due to injector bodies in the open plate configuration is 14% and 12.5% for the strut and ramp injectors, respectively. With the exception of the fuel ports, the grid was clustered toward all of the walls with the growth rates varying from 5%–15%. The values of y^+ for these cases, obtained on a fine mesh, were no greater than 20, with the largest values observed on the injector bodies and fuel port walls. The y^+ values along the flat plate are all less than one. The values of y^+ are about two and four times larger for the medium and coarse meshes, respectively.

A grid dependence study for the open flat plate configurations was previously performed by Drozda et al.⁴ The flow conditions were slightly different than those reported in Table 2 and the fuel used was helium not hydrogen, however, because the mixing flowfields are comparable between helium and hydrogen,³ and the Reynolds numbers are comparable between the current flow conditions and those investigated previously,⁴ this study was deemed sufficient. The observed numerical errors, obtained using the Grid Convergence Index (GCI),²⁵ in the total pressure recovery are typically 1%–2%, with a maximum value of about 5%. Typical errors in the computed mixing efficiencies are about 5%, with maximums up to about 15% (in the near-field of the ramp injector case). Because the differences between the one-dimensional values of the quantities of interest obtained from the simulations on the medium and fine meshes are relatively small, only the results of the simulations obtained on the medium meshes are used in the present work.

For the simulations of the ducted flowpaths, the grids developed for the open flat plate simulations were rotated 180 degrees about an axis positioned 1.5 inches above the flat plate and aligned with the x-direction to form the interdigitated configurations as shown in Figs. 4–6(c). This resulted in a duct height of 3 inches, which is the same as that previously studied by Baurle et al.⁵ The rotation process also doubled the total size of each grid. This increase in the grid size provided further motivation for using only the medium grids in order to reduce the computational costs of the simulations. It should be noted that the flow blockage due to the injector bodies in the duct increased to 26.4% and 25% for the strut and ramp injectors, respectively, as compared to the open flat plate simulations.

RESULTS AND DISCUSSION

This section contains the flow visualizations using the contours of the Mach number and one-dimensional injector performance analysis for the strut, ramp, and flushwall injectors obtained for the open plate and ducted configurations. Both mixing-only and mixing-and-reacting cases are shown for all injectors and configurations. In addition, for the ducted cases, the one-dimensional analysis is also performed for unfueled cases to illustrate the *baseline* level of losses and subsequent impact of fuel injection, mixing, and chemical reactions. Unless otherwise noted, the one-dimensional performance metrics of interest for the open plate configurations have been corrected to the duct height using the area-ratio-based correction approach. However, the uncorrected results and those obtained using the truncated-domain correction approach are also shown for the strut injector only. In addition, for the ramp and flushwall injectors, the area-ratio-based correction was also computed for the IFA, which for those injectors is half the duct height. Correcting to IFA for the strut injector produces the same results as those obtained by correcting to the duct height because the height of the strut IFA is the same as the duct height. However, for the ramp and flushwall injectors, correcting to the IFA has the potential to partially account for the full losses of the duct because the IFA for those injectors is half the duct height and the duct is symmetric about its midplane. This section is organized as follows: each of the three injectors is first discussed individually in the context of open plate and ducted configurations, then one-dimensional performance analysis is presented for all injectors, focusing on the subset of the data to highlight some key takeaways of the analysis.

STRUT INJECTOR

Mach number contours on streamwise planes through the centerline of injector ports, midplanes between the injectors, and cross-stream planes at various downstream locations obtained from the strut injector simulations for the open and ducted cases, are shown in Figs. 7–9. The downstream distance in these figures is in inches, with the black isolines denoting the stoichiometric value of the fuel mass fraction. Both mixing-only and mixing-and-reacting cases are shown. It is clear from these figures that the shock patterns and the fuel-air mixing are quite different between the simulations on the open plate and those in the duct. Although the simulation on the open plate captures the lateral shocks emanating from the leading edge of the strut injector, they do not reproduce the reflected shock patterns present in the ducted simulations. The differences in the mixing are most clearly visualized in Fig. 9. It is clear from observing the fuel-air interface, denoted by the isoline of the stoichiometric value of the mass fraction, that the manner in which fuel and air mix is drastically different. Specifically, while the fuel-air interface spreads mostly laterally for the open flat plate simulations, the same interface exhibits a strong effect of vorticity, induced by the staggering of fuel ports of the adjacent interdigitated strut injectors. The effect of chemical reactions can be observed through the decreases in the value of the Mach number as heat is released into the flow.

The one-dimensional values of the mass-flux weighted Mach number, mixing and combustion efficiencies, total pressure recovery, and the specific thrust potential versus the downstream distance obtained from the strut injector simulations are shown in Fig 10. The values are shown for the mixing-only and mixing-and-reacting cases for both the simulations on the open plate and in the duct, as well as the unfueled case for the ducted cases only. In addition, the left-most column of plots shows the results of the one-dimensional analysis where the simulation data for the open plate case was truncated to match the height of the duct prior to performing the one-dimensional analysis. This was done to investigate the impact of the physical

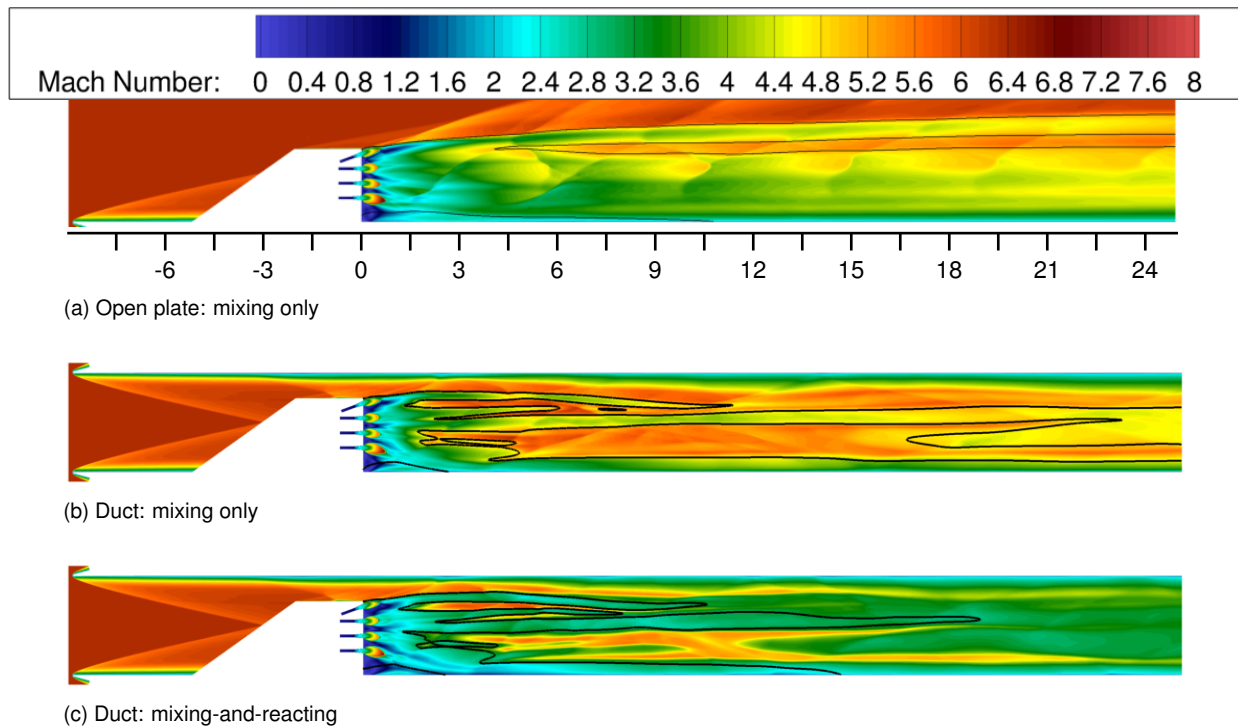


Figure 7. Mach number contours on the streamwise planes through the centerline obtained from the strut injector simulations for the open (a) and ducted (b,c) cases. Downstream distance is in inches. Black lines denote the stoichiometric value of the fuel mass fraction.

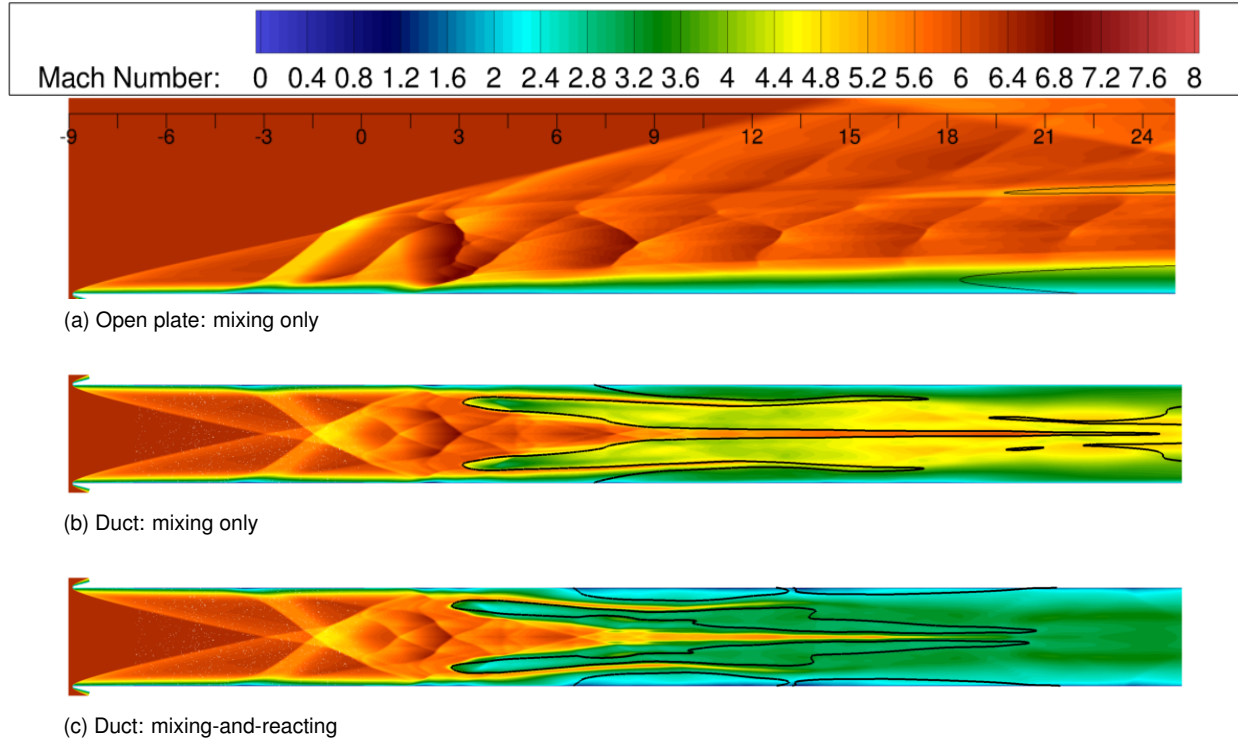


Figure 8. Mach number contours on the streamwise planes through the midplane between the injectors obtained from the strut injector simulations for the open (a) and ducted (b,c) cases. Downstream distance is in inches. Black lines denote the stoichiometric value of the fuel mass fraction.

extent of the analysis domain on the various metrics of interest, and to verify the validity of the area-ratio-based correction approach. That is, the truncated-domain and the area-ratio-based correction approaches must produce the same results up to the point where the flat plate bow shock intersects the truncated plane. However, it should be noted that for the truncated-domain correction approach case, unlike the area-ratio-based corrected case, mass can freely move in and out of the truncated domain, which can impact the one-dimensional analysis results in uncontrolled ways. All of the one-dimensional analysis results are consistent with the general observations of the Mach number contours discussed above. That is, as the fuel is injected and mixes with air and heat from combustion is released into the flow, the Mach number decreases. For the unfueled case, the Mach number increases for a short distance downstream from the end of the injector as the flow accelerates to fill the base region. The increase is gradual because the back face of the injector body produces a wake that mitigates the effect of the discrete area change at the base of the injector. For the fueled cases, this initial increase in the Mach number is reduced by the addition of fuel. The values of the Mach number computed using the area-ratio-based corrected approach and for the truncated-domain correction approach match more closely with those for the ducted case than the uncorrected values, also shown for the open plate configuration, because the freestream values are excluded from those calculations. However, the additional decrease induced by the losses caused by the opposing wall and the resulting shock reflections for the ducted cases are obviously absent in the corrected results. The mixing and combustion efficiency are the highest for the ducted case. The mixing efficiency for the reacting simulations is lower than that for the mixing-only cases due to the combined effect of the heat release and product formation at the fuel-air interface, both of which tend to reduce mixing, and the combustion efficiency is lower than the mixing efficiency by the finite-rate effect of the chemical kinetics. Unlike the Mach number, the mixing efficiency is zero in the freestream, and therefore, truncating the computation domain has little impact on its one-dimensional values. Nevertheless, beginning at about

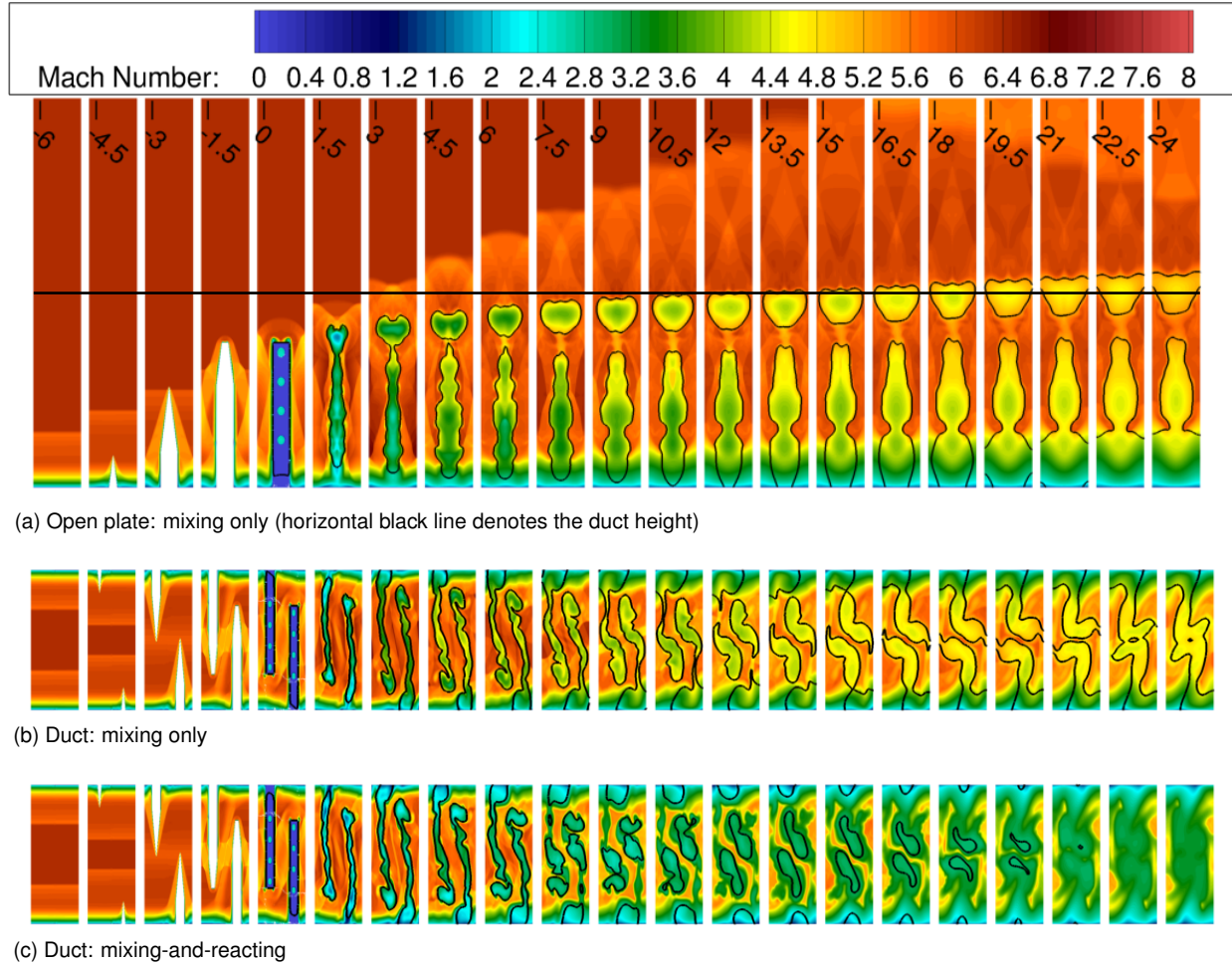


Figure 9. Mach number contours on the cross-stream planes at various downstream locations obtained from the strut injector simulations for the open (a) and ducted (b,c) cases. Downstream distance is in inches. Black lines denote the stoichiometric value of the fuel mass fraction.

x=15 inches, some differences can be observed between the area-ratio-based corrected and truncated results for the open plate case. These differences are the result of the mixing plume that originated from the upper-most fuel port leaving the truncated domain (see Fig. 9(a)). Similar to the Mach number values, the uncorrected total pressure recovery is significantly higher for the open plate simulations. This is due to the absence of the losses caused by the shocks emanating from the upper plate of the duct and the inclusion of the larger flow area, which skews the mass-flux-weighted total pressure values toward the freestream. The total pressure recovery obtained from the area-ratio corrected and truncated-domain open plate data appears closer to that of the ducted data, however, the agreement for the truncated data may be fortuitous. Nevertheless, the values of the total pressure recovery obtained using both the area-ratio corrected and truncated-domain approaches are still higher than those obtained for the duct because of the absence of reflected shock features on the open plate. The specific thrust potential values are comparable between the area-ratio corrected open plate and ducted cases, and the thrust augmentation due to the aft-facing fuel injection is identical in all the cases. However, the mixing, viscous, and shock losses are about 50% larger with respect to the peak value for the ducted case as compared to the area-ratio corrected open plate values. Furthermore, although the thrust potential obtained for the reacting simulations on the open plate monotonically decreases, the same values for the ducted case appear to level off to a constant value. This indicates that the thrust losses due to the viscous effects, mixing, and shock waves have been offset by

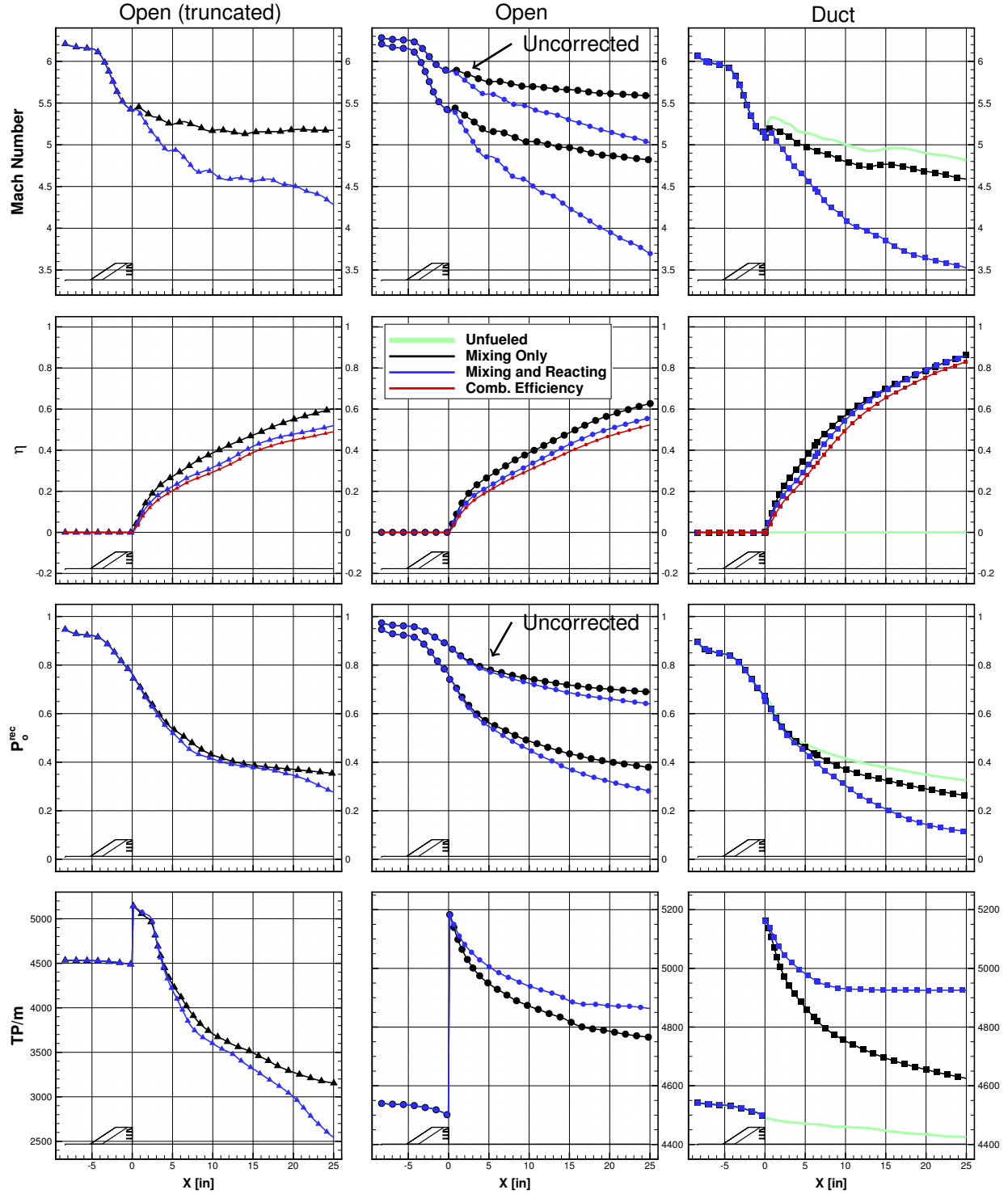


Figure 10. One-dimensional values for the mass-flux weighted Mach number, mixing (and combustion) efficiency, total pressure recovery, and specific thrust potential (in N/(kg/s)) vs. downstream distance obtained from the strut injector simulations for the open, and ducted cases.

the heat release for the ducted case. The thrust potential values for the truncated-domain correction only remain consistent with the other two cases until approximately 2 inches downstream of the injection plane. This location coincides with the point where the shock waves emanating from the injector body move above the duct height mark for the open plate simulations (see Fig. 9(a)). Downstream of this location the thrust significantly decreases. The rate of the decrease is much greater than that for the other cases because the thrust potential is strongly impacted by the injected fuel, and the fuel stream of the top-most fuel port begins to move out of the truncated domain. The truncated-domain one-dimensional results are further shown to be incorrect by the fact that the specific thrust potential is lower for the reacting case. Although this is physically possible and can occur when the mixing and reacting losses occur with minimal heat release to compensate, given the results of the corrected open plate case, this result is clearly a consequence of mass crossing the top boundary of the truncated domain as the fuel-air mixture reacts and expands due to combustion.

An alternative way to illustrate and to compare the total pressure losses and the specific thrust potential between the open plate and ducted cases is to plot these quantities versus the mixing efficiency, as shown in Fig. 11 for the strut injector simulations. Only the area ratio corrected one-dimensional quantities are plotted for the open plate case. In the total pressure recovery plot, an ideal fuel injector would be represented by a nearly horizontal line with a slightly negative slope accounting for only the minimum required fuel-air mixing losses. For realistic injectors, viscous and shock losses further decrease the value of this slope. For the current cases, the amount of total pressure loss per unit mixing (i.e., the slope of the curve) is about the same for the open and ducted cases. Hence, despite the large differences in losses, both configurations are about equally “efficient” at mixing the fuel and air. The downward offset in the value of the total pressure recovery for the ducted results is a result of the greater total pressure losses incurred in the duct as a result of shock features emanating from the second (upper) plate. Nevertheless, these larger losses are indeed converted into greater mixing, as indicated by a larger final value of the mixing efficiency for the ducted case as compared to the open flat plate case. The situation is similar for the specific thrust potential, where the mixing-only cases exhibit a surprisingly comparable rate of thrust production (or loss) per unit mixing. Furthermore, it appears that the additional losses incurred in the duct, when realized as enhanced mixing, do enable higher thrust production, with the thrust potential marginally offsetting the losses for a mixing efficiency value greater than 0.6.

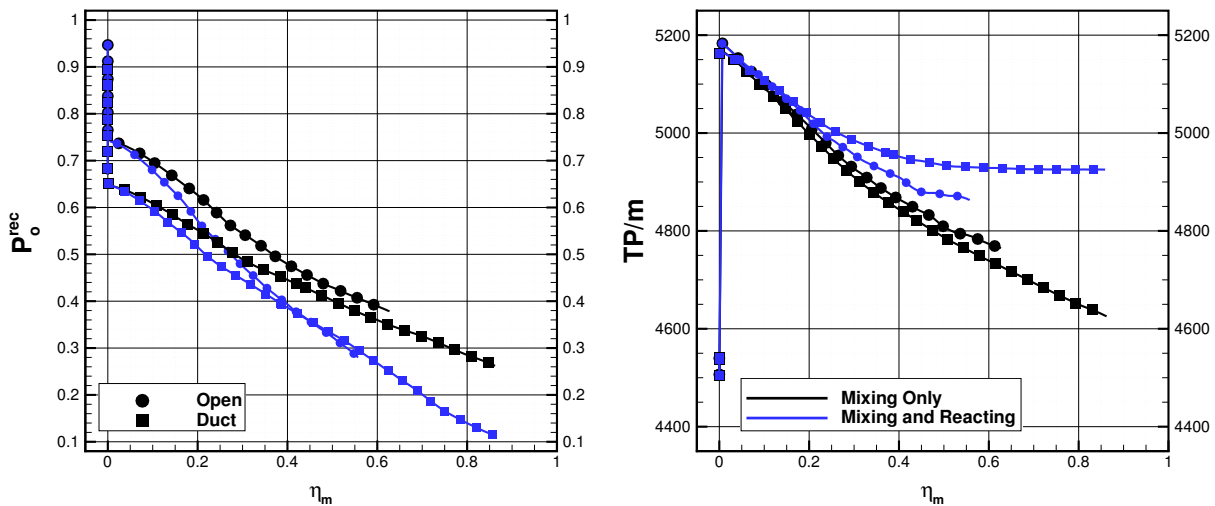


Figure 11. One-dimensional values for total pressure recovery and specific thrust potential (in N/(kg/s)) vs. the mixing efficiency obtained from the strut injector simulations for the open, and ducted cases. The open plate results are corrected to duct height.

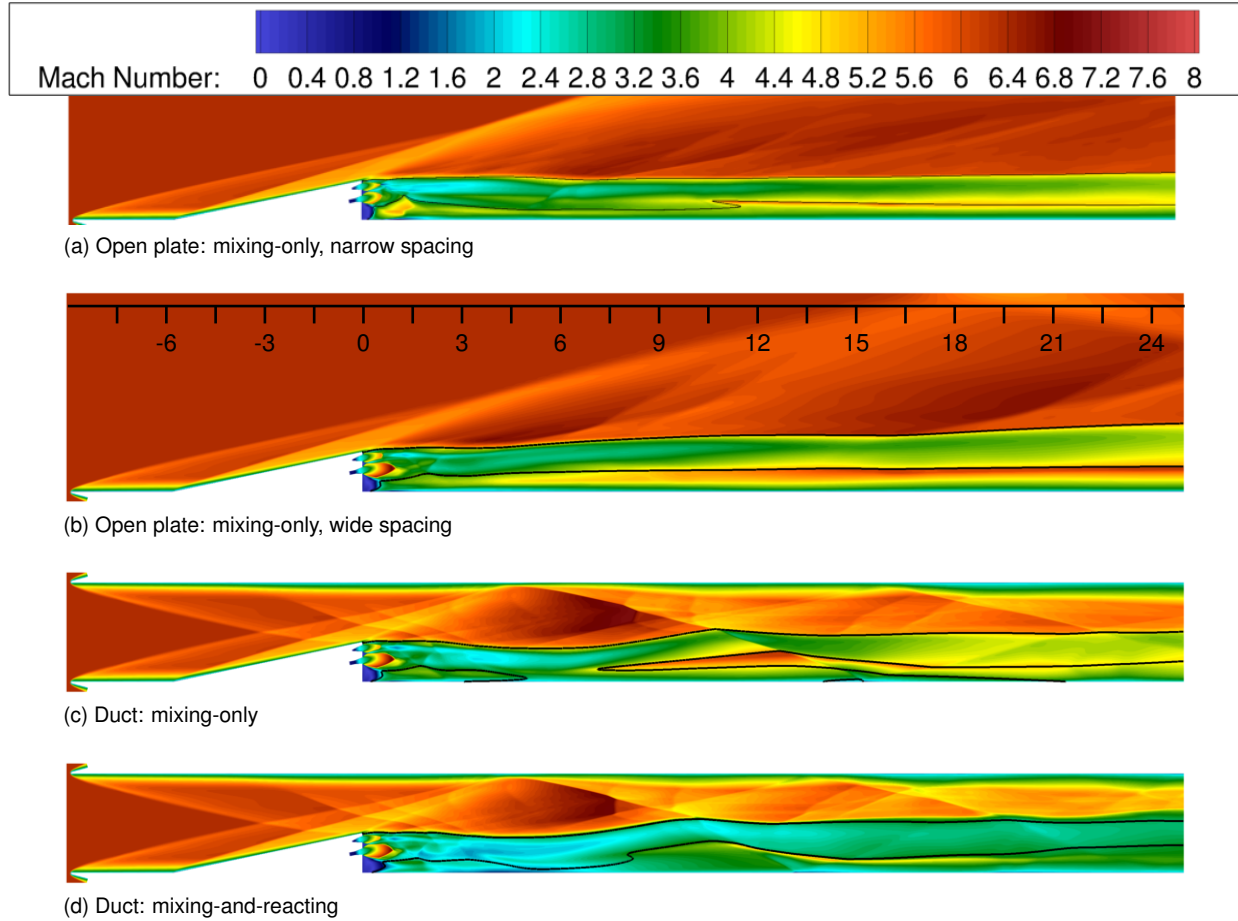


Figure 12. Mach number contours on the streamwise planes through the centerline obtained from the ramp injector simulations for the open (a) and ducted (b,c,d) cases. Downstream distance is in inches. Black lines denote the stoichiometric value of the fuel mass fraction.

RAMP INJECTOR

Mach number contours on streamwise planes through the center of the injector ports, midplanes between the injectors, and cross-stream planes at various downstream locations obtained from the ramp injector simulations for the open and ducted cases are shown in Figs. 12–14. Similar to the comparable plots for the strut injector, the downstream distance in these figures is in inches, with the black isolines denoting the stoichiometric value of the fuel mass fraction. Both mixing-only and mixing-and-reacting cases are shown. In addition, the ramp injector simulations for the open cases were performed for two injector spacings: a narrow spacing with the adjacent injectors spaced at half the distance of those in the duct, and a wide spacing matching that of the injectors in the duct. The reduction in spacing also resulted in halving the IFA, and thereby the fuel mass flow rate for the narrow-spaced, as compared to the wide-spaced configuration. Once again, it is quite clear from these figures that both the shock patterns and the fuel-air mixing are quite different between the simulations on the open plate and those in the duct.

One of the more drastic differences is caused by the interaction of a reflected shock in the duct with the fuel plume (see Fig. 12(c)). This reflected shock is strengthened by the coalescence of the leading edge bow shock and the ramp shock. The reflected shock effectively introduces a turning force that directs the fuel plume toward the center of the duct. By comparison, the fuel plumes for the open plate cases simply

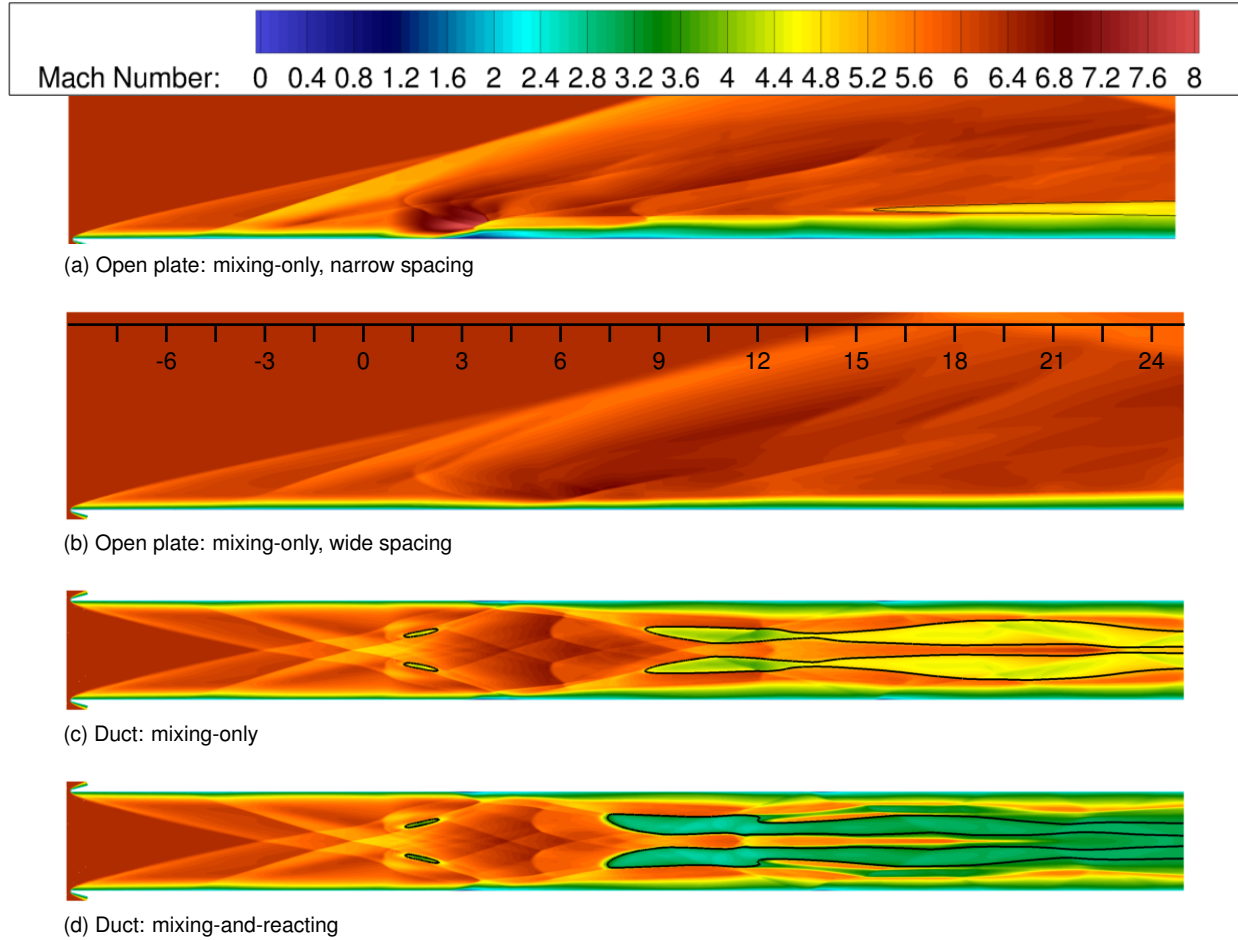
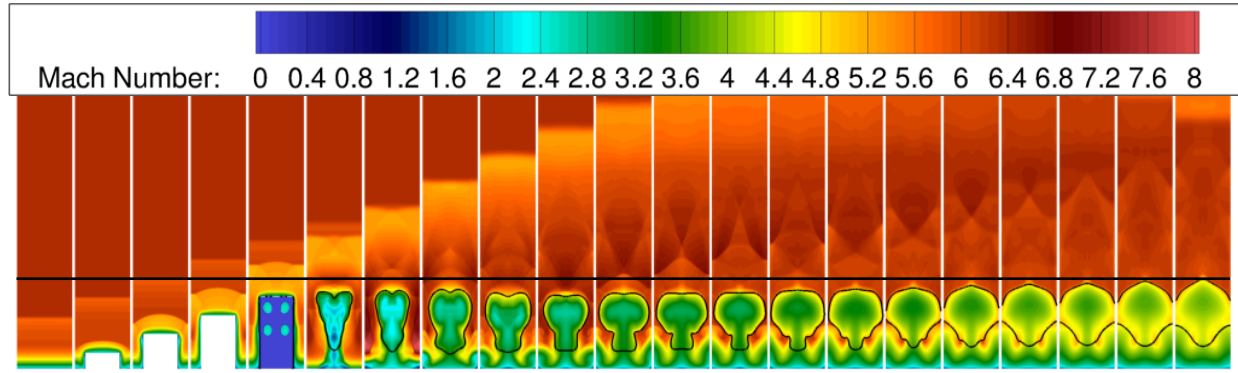


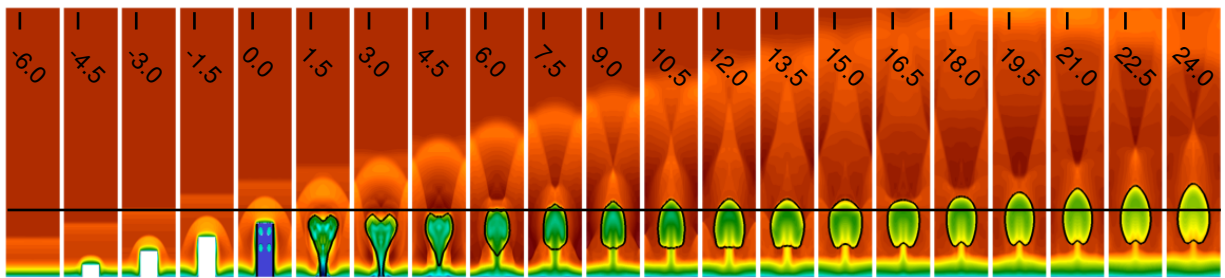
Figure 13. Mach number contours on the streamwise planes through the midplane between the injectors obtained from the ramp injector simulations for the open (a) and ducted (b,c) cases. Downstream distance is in inches. Black lines denote the stoichiometric value of the fuel mass fraction.

diffuse outward from the fuel core, with the primary difference between them being the suppressed upward penetration for the narrow-spaced ramp injectors due to the weaker CVP. This is not surprising because the reduction in injector spacing effectively limits the size and the strength of the CVP. In addition, the reduced mass flow rate of fuel for the narrow-spaced case decreases the momentum flux, and therefore, penetration of the up and outward-pointing fuel ports. However, since the up-and-outward angles of the ramp fuel ports are small with respect to the xz - and xy -planes, respectively, this effect is expected to be small. The Mach number contours obtained at the midplanes further show the differences in the shock structures between the open and ducted cases, with the ducted cases showing that by about 9 inches downstream of the injector, the fuel-air plumes have begun to spread laterally. It should be noted that because the injectors in the duct are interdigitated, the midplane between them is the same distance from the center of the injectors as that for the narrow-spaced injectors on the open plate. The midplane for the wide-spaced injectors on the open plate is effectively twice as far from the center of the injectors as in the interdigitated ducted configuration.

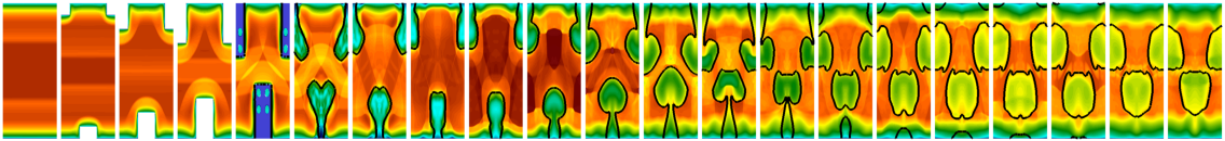
The differences in the mixing are once again most clearly visualized in Fig. 14. It should be noted that for these cross-stream planes, the aspect ratio is not one, and varies between narrow- (open plate) and wide-spaced (both open plate and ducted) configurations to accommodate the same number of downstream planes. It should also be noted that although the shock patterns are quite different between the open



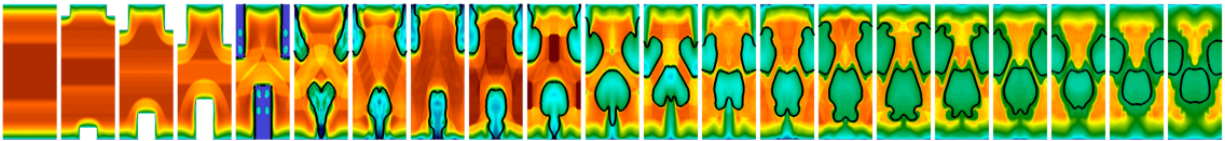
(a) Open plate: mixing-only, narrow spacing (horizontal black line denotes the duct half-height)



(b) Open plate: mixing-only, wide spacing (horizontal black line denotes the duct half-height)



(c) Duct: mixing-only



(d) Duct: mixing-and-reacting

Figure 14. Mach number contours on the cross-stream planes at various downstream locations obtained from the ramp injector simulations for the open (a) and ducted (b,c) cases. Downstream distance is in inches. Black lines denote the stoichiometric value of the fuel mass fraction.

and ducted cases, the mixing plumes, as denoted by the stoichiometric isoline of the fuel mass fraction, are comparable up to about 3 inches downstream (near field) from the injector. One interesting difference between the open and ducted cases is that the fuel plume appears to remain off the wall for the open plate simulations, whereas for the ducted cases, some of the fuel that is entrained into the boundary layer in the near field of the injector remains there. It should also be noted that visual inspection of the cross-stream planes at the locations furthest downstream reveals that the ramp injectors in the ducted configuration might have a spacing that is too wide because the fuel plumes do not cover the IFA and the large-scale vortical structures have saturated. This is further supported by the reacting simulations, where at downstream locations relatively large regions of high Mach number air can be observed moving around centrally-located

slower fuel plumes. The extent of reaction is also observed in the cross-stream planes through the decrease in the values of the Mach number as heat is released into the flow.

The one-dimensional values of the mass-flux weighted Mach number, mixing and combustion efficiencies, total pressure recovery, and the specific thrust potential versus the downstream distance obtained from the ramp injector simulations are shown in Fig 15. The data are shown for the mixing-only and mixing-and-reacting cases for the simulations on the open plate and in the duct, as well as the unfueled case for the ducted cases only. In addition, the left column of plots show the results for the narrow-spaced ramp injectors. This was done to investigate the impact of the injector spacing and the size of the IFA on the various metrics of interest. Furthermore, the open plate data for the wide-spaced ramp injectors have also been corrected with respect to the IFA to illustrate the difference between the two area corrections. Because the height of the IFA for the ramp injector is equal to half the duct height, correcting the one-dimensional quantities this way should (because of the duct symmetry about the midplane) partially reproduce the impact of the bow shock and the viscous and mixing losses of the second plate. Nevertheless, the losses due to the shock reflections and any resulting mixing enhancement cannot be captured this way, simply because those physics are absent from the open plate simulations. The one-dimensional analysis results are consistent with the general observations of the Mach number contours discussed above. That is, as the fuel is added and mixes with air and heat is released from chemical reactions, the Mach number decreases. It should be noted that the Mach number corrected to the IFA is a good approximation of the Mach number computed for the ducted cases. The mixing and combustion efficiencies are highest for the ducted case. This results in the largest total pressure losses, although it should be noted that the values of the total pressure recovery corrected to the IFA are a good approximation to the ducted values. The specific thrust potential values are comparable between the open plate and ducted cases. The thrust augmentation due to aft-facing fuel injection is nearly identical for the open and ducted cases. This may be surprising given the fact that the fuel flow rate for the narrow-spaced injectors is half that for the wide-spaced injectors. However, it should be noted that a specific thrust potential is plotted here. Therefore, although the fuel flow rate per injector is reduced, the air mass flow rate per injector is also proportionally reduced such that, per unit mass of air, the thrust augmentation remains the same for all the configurations. The mixing, viscous, and shock losses induce thrust potential losses that are about 20% larger for the ducted case as compared to the open plate cases. The specific thrust potential decreases monotonically for all the cases including the reacting ones. This indicates that the thrust losses due to the viscous effects, mixing, and shock waves have not been offset by the heat release. However, this does not mean that the ramp injector induces more losses than the strut, actually the opposite is true, but only that the fuel-air mixing rate is not sufficient to allow for heat release to balance the losses in thrust potential. As was noted in the strut injector case, a mixing efficiency of about 0.6 or more was required to marginally offset the losses.

The one-dimensional values of the total pressure recovery and specific thrust potential versus the mixing efficiency are shown in Fig. 16 for the ramp injector simulations. For these cases, the amount of total pressure loss per unit mixing (i.e., the slope of the curve) is once again comparable. Furthermore, the “most efficient” mixing occurs for the slowest mixing, wide-spaced, injectors in the open plate configuration. Although the total pressure losses seem to accelerate with mixing for all cases at a mixing efficiency value of about 0.1, the thrust potential changes at about the same rate for the wide-spaced injectors on the open plate and in the ducted configuration. What makes this plot interesting, however, is the fact that, with the exception of regions with high values of the mixing efficiency for the ducted case, the mixing-and-reacting thrust potential values are almost on top of each other. This indicates that the gain from the heat release due to combustion just barely offsets the losses due to the chemical reactions, while viscous and shock losses continue to decrease the thrust potential.

FLUSHWALL INJECTOR

Mach number contours on the streamwise planes through the centerline of the injector, midplanes between the injectors, and cross-stream planes at various downstream locations obtained from the flushwall injector simulations for the open and ducted cases are shown in Figs. 17–19. As before, the downstream distance

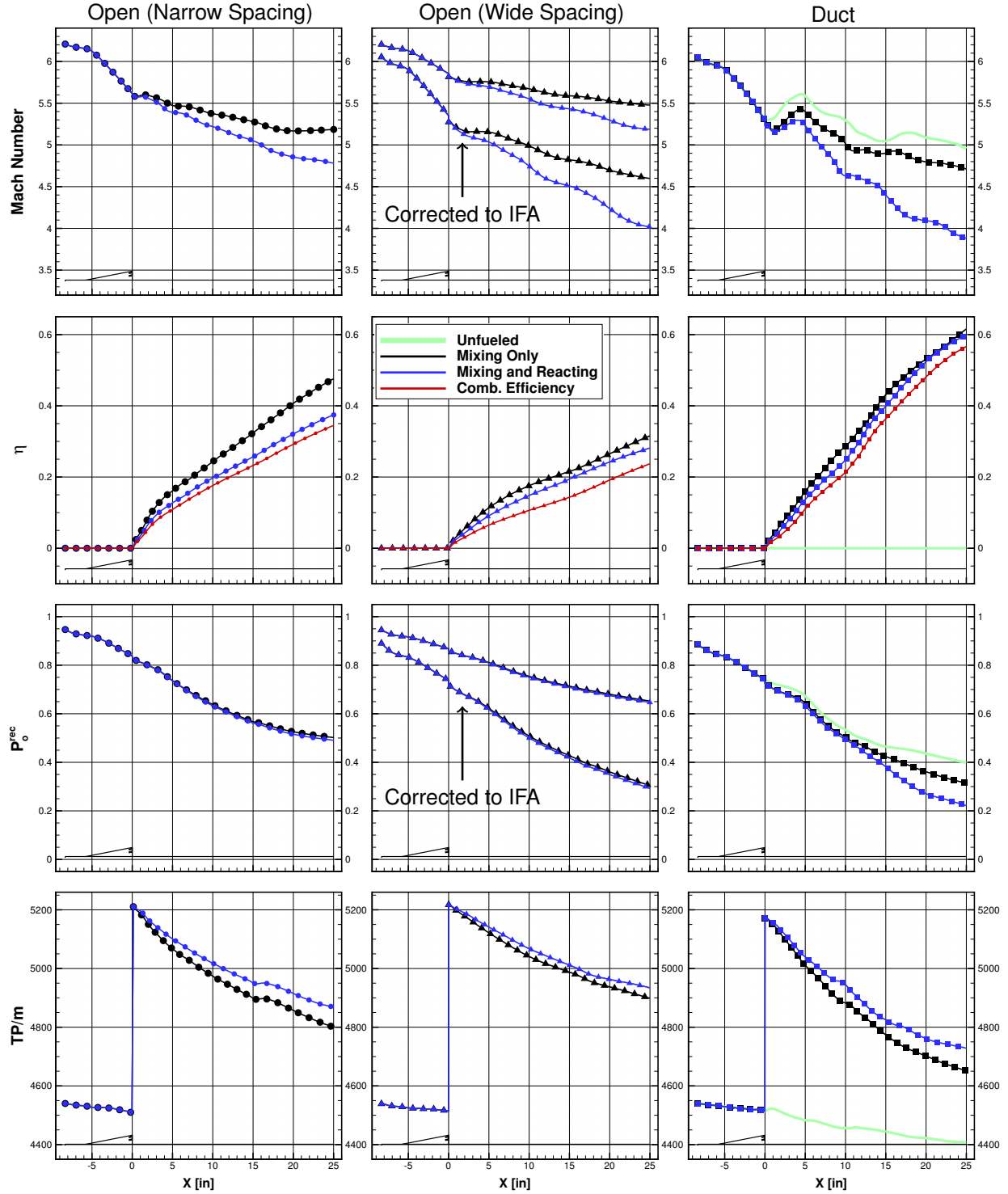


Figure 15. One-dimensional values for the mass-flux weighted Mach number, mixing (and combustion) efficiency, total pressure recovery, and specific thrust potential (in N/(kg/s)) vs. downstream distance obtained from the ramp injector simulations for the open, and ducted cases.

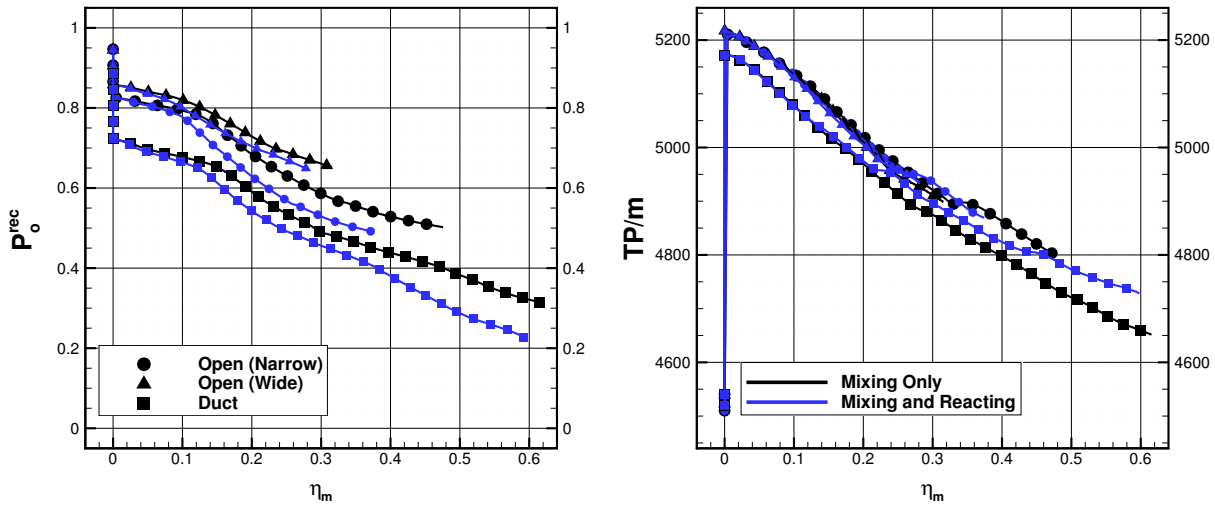


Figure 16. One-dimensional values for total pressure recovery and specific thrust potential (in N/(kg/s)) vs. the mixing efficiency obtained from the ramp injector simulations for the open, and ducted cases.

in these figures is in inches, with the black isolines denoting the stoichiometric value of the fuel mass fraction. Both mixing-only and mixing-and-reacting cases are shown. In addition, similar to the open cases for the ramp injector, the open cases for the flushwall injector were performed for two injector spacings: a narrow spacing with the adjacent injectors spaced at half the distance of those in the duct, and wide spacing matching that of injectors in the duct. As before, the IFA and the fuel mass flow rate are reduced for the individual narrow-spaced injectors. In general, the flowfield is somewhat similar to that for the ramp injector. Instead of a ramp shock, the fuel plume introduces a bow shock. Because the fuel penetration is proportional to the dynamic pressure ratio, the plume penetration is reduced for the narrow-spaced injectors on the open plate. The ducted cases in Fig. 17(c,d), indicate the impact of the reflected shocks on both the opposite wall boundary layer and the fuel-air mixing plume. In the manner similar to that of the ramp injector, the shock waves that form around the fuel plume (or ramp injector body) and the reflected bow shock of the flat plate form a complex pattern of compressions and expansions that interact downstream with the fuel plume and cause it to rise and drop as it is processed by these compressible flow features. The Mach number contours obtained at the midplanes further show the differences in the shock structures between the open and ducted cases. In addition, the lateral fuel spreading is most pronounced for the ducted cases. The similarities and differences in the mixing are most clearly visualized in Fig. 19. Because the interactions between the lower and upper fuel plumes in the duct are limited, the mixing plumes are quite comparable between those on the open plate and in the duct. Any differences between the open plate and ducted cases are due to the interaction of the shock waves reflected in the duct with the fuel plumes. Clearly this injector is not optimized for use in the ducted configuration because neither the penetration nor the lateral spreading are sufficient to take advantage of the potential interactions offered by the interdigitated configuration. As with the previous two injectors, the reacting simulations reveal reduced values of the Mach number near the stoichiometry.

The one-dimensional values of the mass-flux weighted Mach number, mixing and combustion efficiencies, total pressure recovery, and the specific thrust potential versus the downstream distance obtained from the flushwall injector simulations are shown in Fig 20. As for the ramp, the data are shown for the mixing-only and mixing-and-reacting cases for the simulations on the open plate and in the duct, as well as for the unfueled case for the ducted cases only. In addition, the left column of plots shows the results of the one-dimensional analysis for the narrow-spaced flushwall injectors. Furthermore, the open plate data for the wide-spaced flushwall injectors have also been corrected with respect to the IFA. Unique to the flushwall

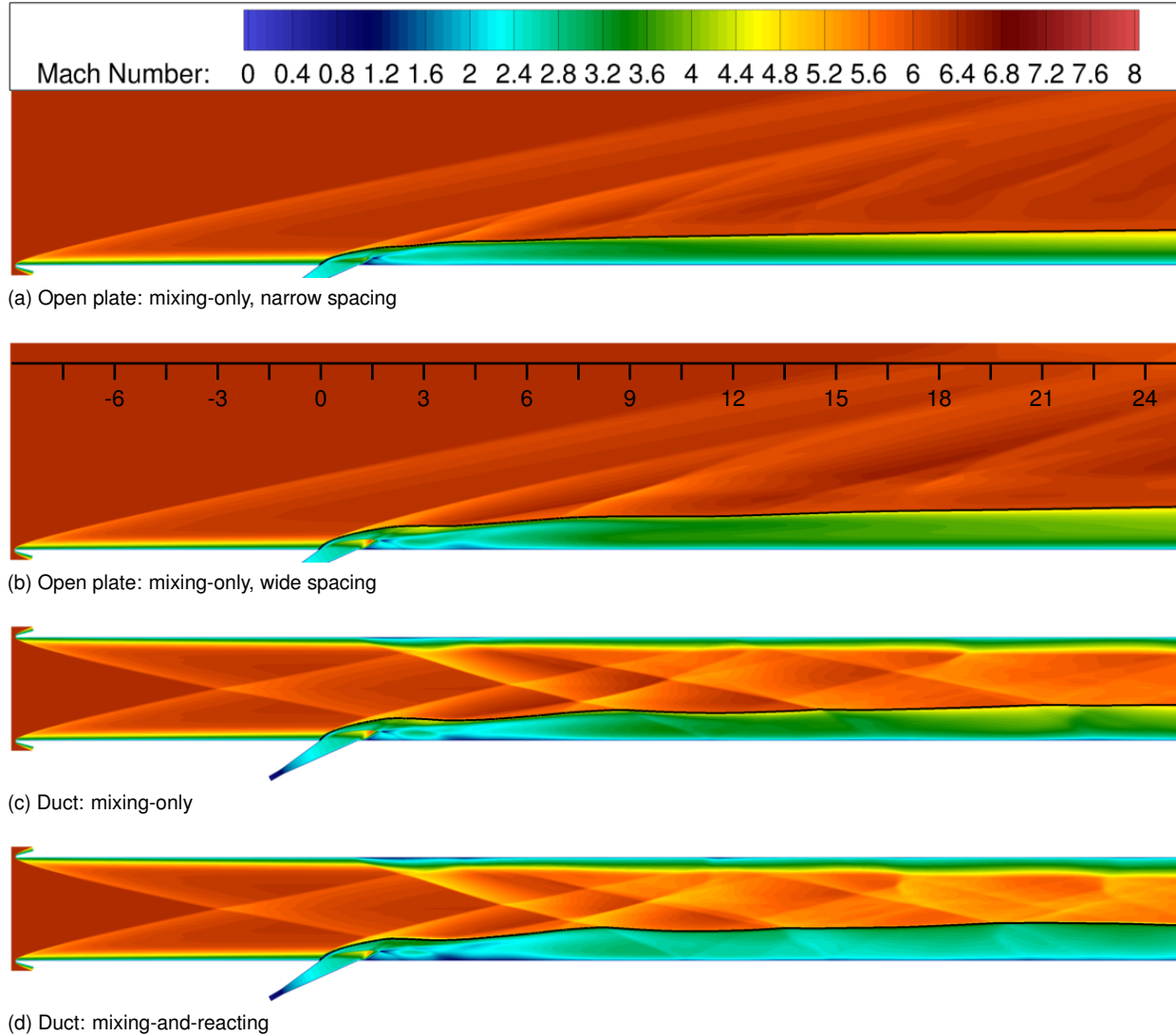


Figure 17. Mach number contours on the streamwise planes through the centerline obtained from the flushwall injector simulations for the open (a) and ducted (b,c,d) cases. Downstream distance is in inches. Black lines denote the stoichiometric value of the fuel mass fraction.

injector is a relatively large decrease in the value of the Mach number and total pressure recovery for the mixing-and-reacting cases as compared to the unfueled case. However, this is simply because the flushwall injector does not introduce any obstruction or blockage into the flow until the fuel is turned on, at which point, a bow shock forms upstream of the fuel injection site. Because the interactions between the lower and upper fuel plumes are limited for the ducted cases, the mixing and combustion efficiencies compare more favorably between the cases. Nevertheless, the interactions between the reflected shocks and the fuel plumes in the duct, although adding losses, still serve to enhance mixing, such that it is largest for the ducted case. This also results in the largest total pressure losses, although it should be noted once more that the values of the total pressure recovery corrected to the IFA provide a very good approximation to the values obtained for the ducted case. The specific thrust potential values are comparable between the open plate and ducted cases. The thrust augmentation due to aft-inclined angled fuel injection is identical for the open and ducted cases. Similar to the ramp case, the mixing, viscous, and shock losses are about 20% larger for the ducted case as compared to the open plate values. The specific thrust potential decreases

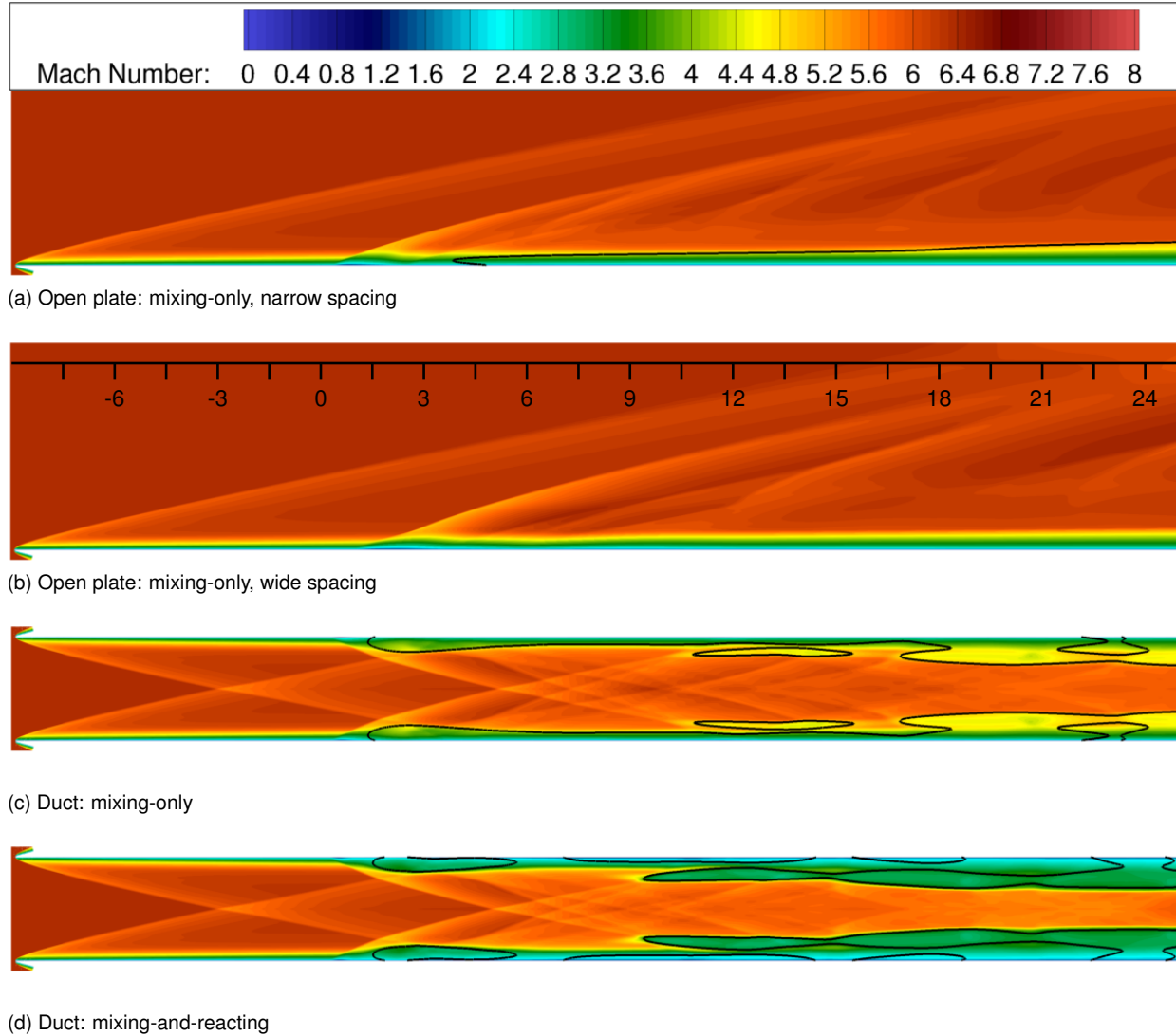
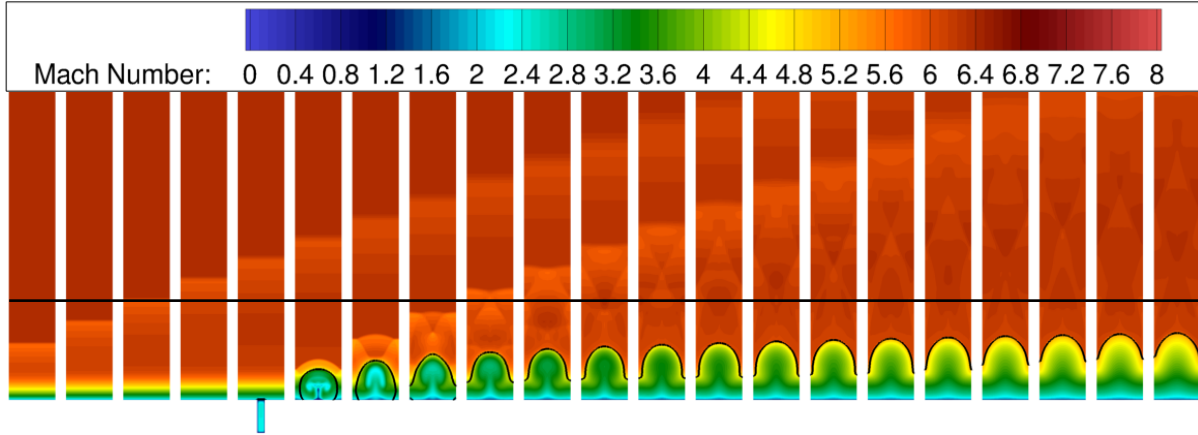


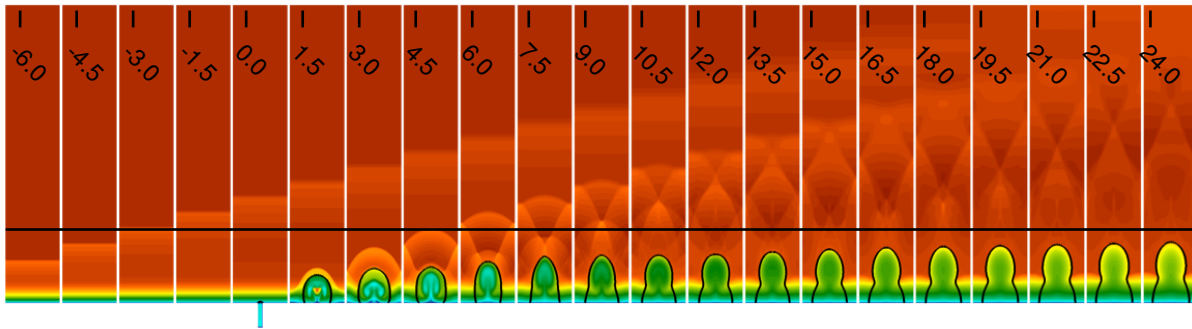
Figure 18. Mach number contours on the streamwise planes through the midplane between the injectors obtained from the flushwall injector simulations for the open (a) and ducted (b,c) cases. Downstream distance is in inches. Black lines denote the stoichiometric value of the fuel mass fraction.

monotonically for all the cases including the reacting ones. This indicates that the thrust losses due to the viscous effects, mixing, and shock waves have not been sufficiently offset by the heat release.

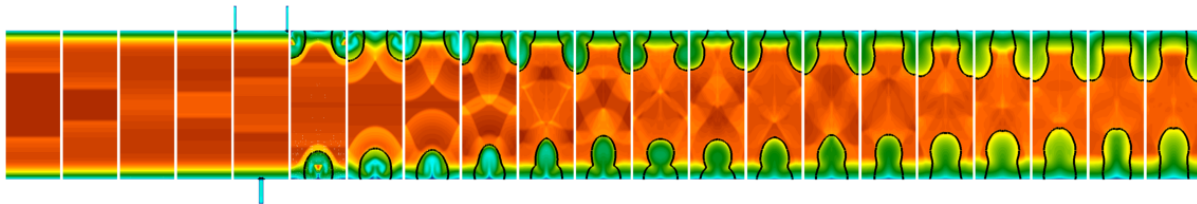
The one-dimensional values of the total pressure recovery and specific thrust potential versus the mixing efficiency are shown in Fig. 21 for the flushwall injector simulations. For these cases, the amount of total pressure loss per unit mixing (i.e., the slope of the curve) is comparable. For the ducted case, the larger initial drop in the total pressure recovery is due to the losses from the second plate upstream of the injection. In addition, once the fuel-air mixing begins, the initial total pressure recovery decreases more rapidly for the ducted cases. This indicates that losses are incurred without the corresponding enhancement to the fuel-air mixing, as was the case for the other injectors. The decrease in the total pressure recovery for all cases is most rapid for values of mixing efficiency less than 0.1, or up to about 5 inches downstream from the injection plane. A detailed investigation as to the specific reasons for this behavior will be conducted in



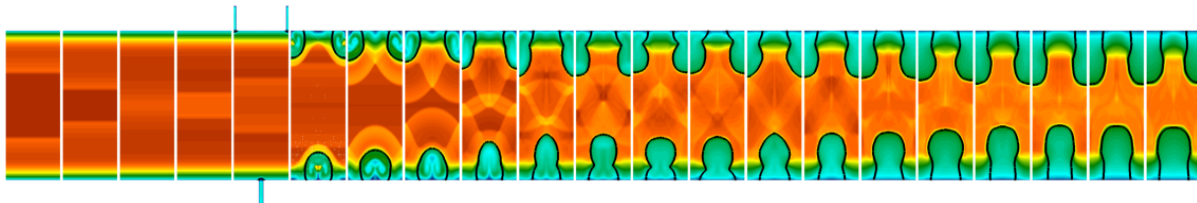
(a) Open plate: mixing-only, narrow spacing (horizontal black line denotes the duct half-height)



(b) Open plate: mixing-only, wide spacing (horizontal black line denotes the duct half-height)



(c) Duct: mixing-only



(d) Duct: mixing-and-reacting

Figure 19. Mach number contours on the cross-stream planes at various downstream locations obtained from the flushwall injector simulations for the open (a) and ducted (b,c) cases. Downstream distance is in inches. Black lines denote the stoichiometric value of the fuel mass fraction.

the future. Currently, it is unclear what physical mechanisms, not also present in the open plate cases, are responsible for this effect. Another notable feature is that the most efficient mixing occurs for the narrow-spaced injectors in the open plate configuration. Furthermore, unlike the other injectors where more efficient

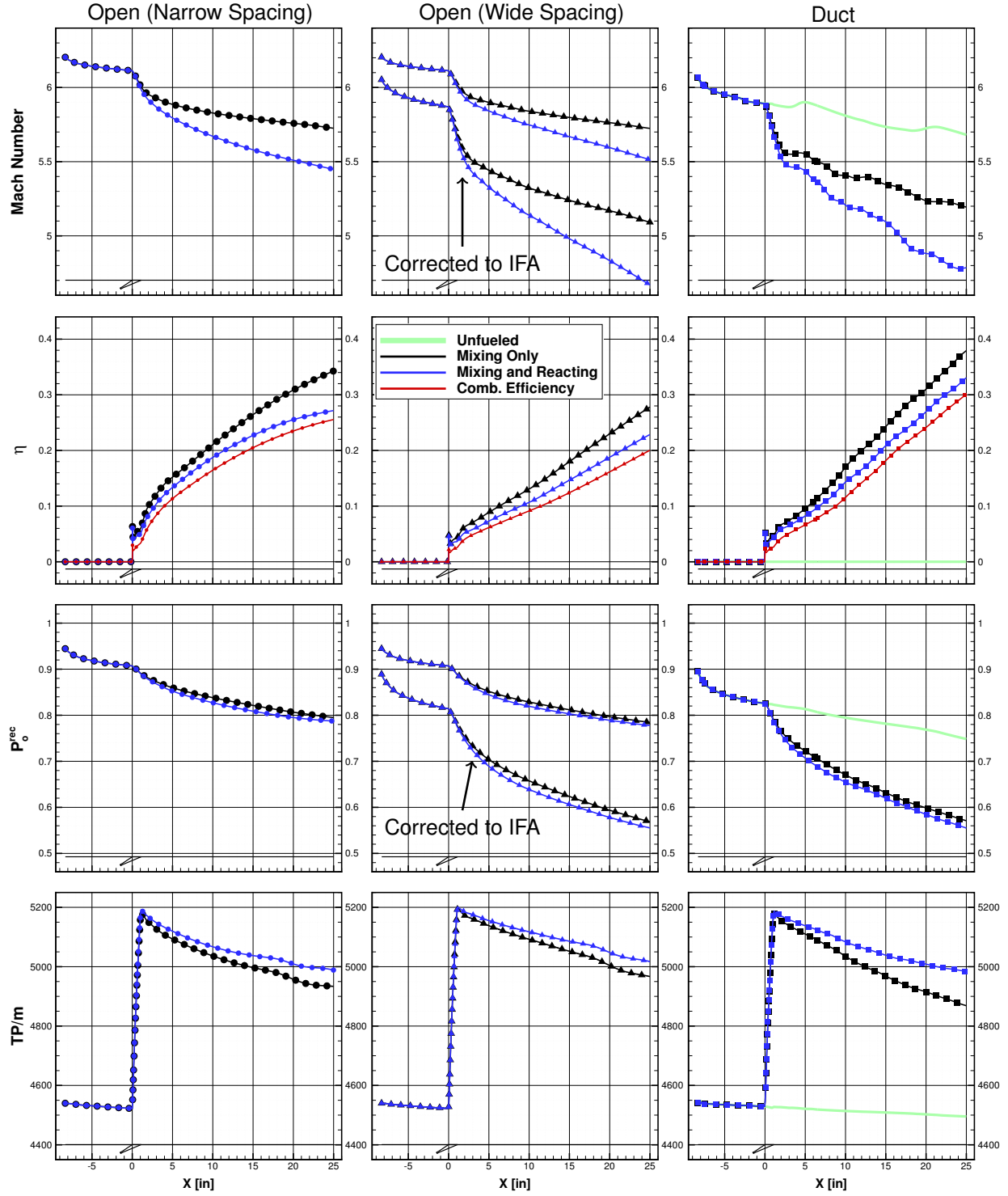


Figure 20. One-dimensional values for the mass-flux weighted Mach number, mixing (and combustion) efficiency, total pressure recovery, and specific thrust potential (in N/(kg/s)) vs. downstream distance obtained from the flushwall injector simulations for the open, and ducted cases.

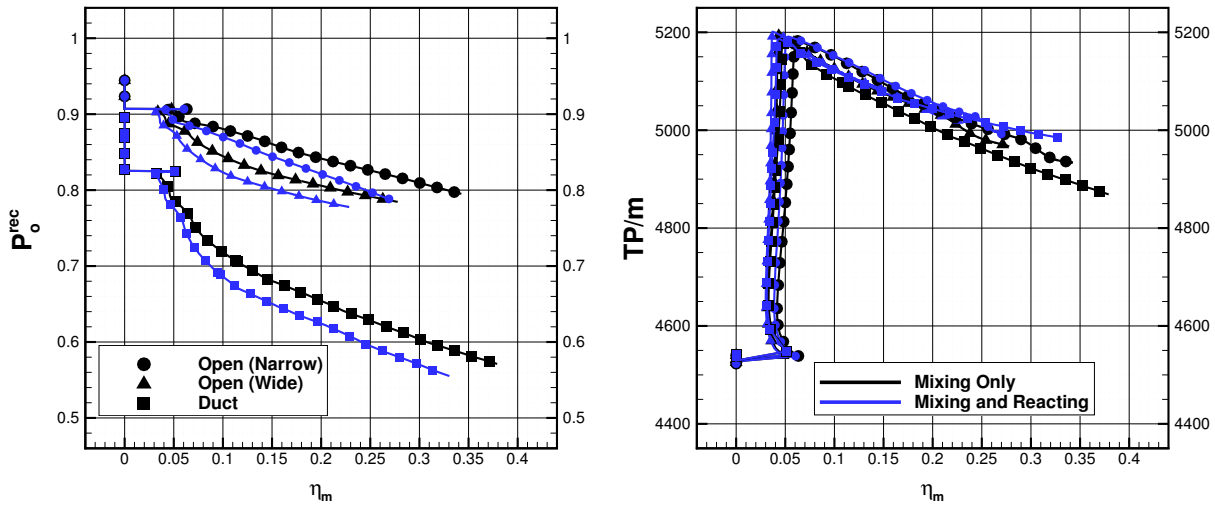


Figure 21. One-dimensional values for total pressure recovery and specific thrust potential (in N/(kg/s)) vs. the mixing efficiency obtained from the flushwall injector simulations for the open, and ducted cases.

mixing typically resulted in a lower value for the maximum mixing efficiency, for the narrow-spaced flushwall injectors, the mixing is not only more efficient, but also more rapid. This indicates a truly higher mixing performance for this case. Although the total pressure losses are accelerated with mixing in the near-field, with the largest decreases for the ducted configuration, the specific thrust potential changes at about the same rate for the injectors on the open plate and in the ducted configuration. Similar to the other injectors cases, the rate of thrust losses with mixing is the same for the current cases. In addition, with the exception of the ducted case, the mixing-and-reacting thrust potential values are almost on top of each other. This indicates that the heat release due to combustion just barely offsets the total pressure losses due to the chemical reactions.

ALL INJECTORS

To facilitate easy comparisons among the injectors, the one-dimensional values of the mass-flux weighted Mach number, mixing efficiency, total pressure recovery, and specific thrust potential versus the downstream distance obtained from the wide-spaced open plate and ducted simulations are shown in Fig 22. Only the data for the mixing simulations are shown because the reacting cases exhibit similar trends. In these plots, the quantities obtained from the open plate simulations have been corrected to the duct height. The trends between the open plate and ducted cases for all of the quantities are similar with the largest discrepancies occurring for the ramp injector. On the open plate, the mixing efficiency for the ramp injector case is similar to that for the flushwall injector, whereas in the duct, the ramp injector mixes the fuel and air much more rapidly than the flushwall injector starting at about 3-4 inches downstream of the injection plane. This location also coincides with a rise in the Mach number in the duct likely due to a complex interaction of the reflected shocks and expansions with the mixing plume. These interactions sustain the near field rate of mixing in the duct, whereas their absence causes the mixing rate to decrease on the open plate. The total pressure recovery trends are also similar between the open plate and duct cases for the strut and flushwall injectors. The rapid decrease in the total pressure in the duct for the ramp injector after approximately 5 inches downstream of the injection plane is due to the reflected shock, which is absent in the open plate cases. Lastly, because mixing is enhanced for all injectors in the duct by the interactions of the fuel plumes with the reflected shocks and additional flow distortions induced by the interdigitation, the thrust potential

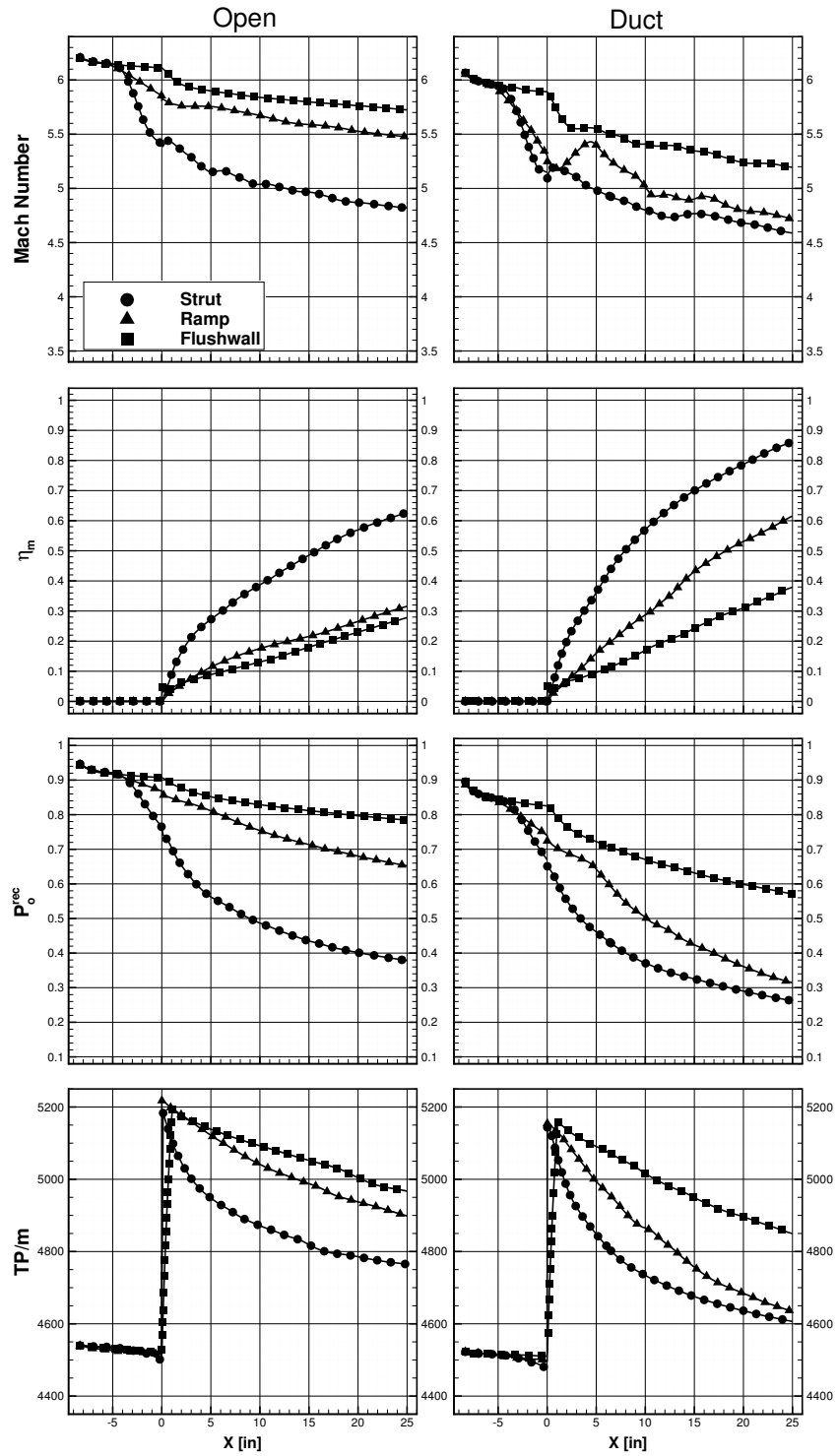


Figure 22. One-dimensional values for the mass-flux weighted Mach number, mixing efficiency, total pressure recovery, and specific thrust potential (in N/(kg/s)) vs. downstream distance obtained from the mixing-only simulations for all injectors for the open, and ducted cases.

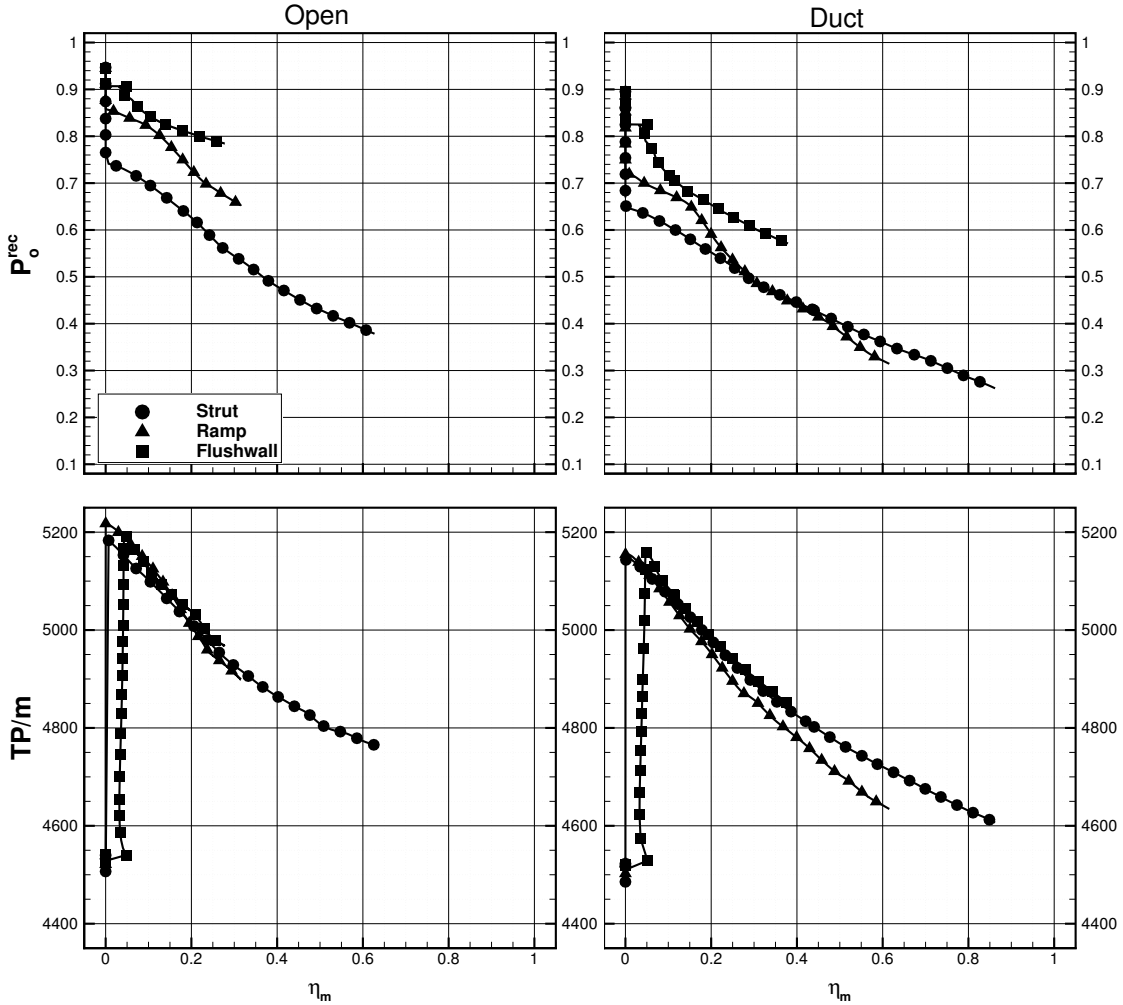


Figure 23. One-dimensional values for total pressure recovery and specific thrust potential (in N/(kg/s)) vs. the mixing efficiency obtained from the mixing-only simulations for all injectors for the open, and ducted cases.

is necessarily reduced. Despite the differences, the “ranking” of injectors with respect to any quantity of interest at every streamwise location is consistent between the open plate and ducted cases.

The one-dimensional values of the total pressure recovery and the specific thrust potential versus the mixing efficiency are shown in Fig. 23 for all of the injectors and open plate and ducted configurations. The rate of the total pressure loss with mixing (slope of the curves in these plots) is comparable among the injectors. This rate is approximately constant for the strut injector, increases downstream of the injection plane for ramp injector, and increases in the near field and levels off to a constant value downstream for the flushwall injector. In general, for all injectors, larger total pressure losses result in higher final values for the mixing efficiency. However, this is not the case for the ramp injector in the duct where total pressure losses surpass those for the strut, yet mixing efficiency remains lower. This suggests that the losses may be occurring away from the fuel plume and therefore, have limited (or no) impact on the mixing. The specific thrust potential decreases at about the same rate for all the injectors on the open plate. The situation is similar for the strut and flushwall injectors in a duct, however, the thrust potential decreases faster with increasing mixing efficiency for the ramp injector. This is consistent with the behavior of the total pressure recovery and

indicates that for the ramp injector more losses do not result in a corresponding mixing and thrust potential enhancement.

SUMMARY AND CONCLUSIONS

The CFD analysis based on Reynolds-averaged simulations (RAS) is presented for the mixing characteristics, performance, and trade-offs of three types of fuel injectors at hypervelocity flow conditions. The primary goal of the current work is not to pinpoint the best fuel injector for hypervelocity flow applications, but rather to discuss physical considerations, and to illustrate and highlight the many competing factors related to fuel injection that may impact the eventual injector performance at any flow condition. The injectors used in this work consist of a fuel placement device, a strut; a fluidic vortical mixer, a ramp; and a flushwall injector. The strut injector has a slender swept body protruding into the core of the flowpath, the ramp injector produces a large vortex, and the flushwall injector is a downstream-oriented high-aspect-ratio rectangle inclined to the wall to augment the thrust. These choices represent three main categories of injectors typically considered in the propulsive devices used for high-speed flight. The mixing characteristics exhibited by these devices when installed on an open plate and in an interdigitated configuration in a duct were compared. The Mach number contours obtained from the RAS revealed the qualitative mixing characteristics for the three injectors in the two configurations. Not surprisingly, it was found that the reflected shock waves, as well as injector interdigitation in the ducted configurations, significantly impacted the flow structures and introduced additional flow features and distortions not observed in the open plate mixing simulations. These additional features were, in general, the result of the interactions between the fuel plumes injected from the lower and upper walls of the duct and interactions between the fuel plumes and the reflected inflow bow shocks. Such interactions are not reproducible in the open plate experiments. The one-dimensional values of the mass-flux-weighted average Mach number, mixing efficiencies, total pressure recovery, and specific thrust potential were used to quantify the differences among the injectors and configurations. A correction process was applied to the quantities obtained for the open flat plate configurations so they could be compared more fairly with the same quantities obtained from the ducted configurations. The correction based on truncating the open plate analysis domain to the duct height before performing one-dimensional analysis proved unable to accurately represent the ducted quantities. However, a correction to the open plate data based on ratios of the areas for the open and ducted flowpaths reasonably captured the trends of quantities in the duct. The one-dimensional quantities showed that although the strut injector produced the greatest amount of fuel-to-air mixing, it did so at the expense of significant total pressure losses. Nevertheless, when combustion was allowed to take place in the simulations, the additional losses to the thrust potential, observed in the mixing simulations, were offset by the heat released by the well-mixed and reacted fuel and air. On the other hand, although the ramp and flushwall injectors exhibited less total pressure loss, they also produced less mixing, which led to less heat release from reactions and consequently monotonically decreasing thrust potential. The one-dimensional plots of the total pressure recovery and thrust potential versus the mixing efficiency showed that the total pressure recovery and thrust potential “efficiency” rates (i.e., the slope of these curves) for the open plate and ducted configurations are comparable for all injectors. This suggests that knowledge about these efficiency rates obtained from ground experiments could potentially be combined with the estimates of the mixing efficiency curves for the conditions of interest to obtain estimates of the total pressure losses. Furthermore, the comparative analysis of all the injectors on the open plate and ducted configurations revealed that, for the current flow conditions, the “ranking” of the injectors with respect to any one-dimensional quantity at any downstream plane was consistent between the open plate and ducted cases. However, it would be prudent to verify that these rankings are indeed consistent even when the fuel-to-air mixing efficiency saturates (i.e., approaches one). Future work will utilize the current injectors in the ducted configuration at a lower Mach number flight condition to assess the injector performance when positive thrust is expected to be generated due to the heat release. This future work would, in addition, evaluate whether the current corrections and the conclusions about the efficiency rates also apply for flow conditions where mixing becomes saturated.

ACKNOWLEDGMENTS

This work is supported by the Hypersonic Technology Project in the Advanced Air Vehicles Program of the NASA Aeronautics Research Mission Directorate (ARMD). Computational resources are provided by the NASA Langley Research Center and the NASA Advanced Supercomputing (NAS) Division.

REFERENCES

- [1] Lee, J., Lin, K.-C., and Eklund, D., **Challenges in Fuel Injection for High-Speed Propulsion Systems**, AIAA J., 53(6):1405–1423 (Jun. 2015).
- [2] Cabell, K., Drozda, T. G., Axdahl, E. L., and Danehy, P. M., **The Enhanced Injection and Mixing Project at NASA Langley**, in *JANNAF 46th CS / 34th APS / 34th EPSS / 28th PSHS Joint Subcommittee Meeting*, Albuquerque, NM (Dec. 2014).
- [3] Drozda, T. G., Baurle, R., and Drummond, J. P., **Impact of Flight Enthalpy, Fuel Simulant, and Chemical Reactions on the Mixing Characteristics of Several Injectors at Hypervelocity Flow Conditions**, in *63rd JANNAF Propulsion Meeting / 47th CS / 35th APS / 34th EPSS / 29th PSHS Joint Subcommittee Meeting*, Newport News, VA (May 2016).
- [4] Drozda, T. G., Drummond, J. P., and Baurle, R. A., **CFD Analysis of Mixing Characteristics of Several Fuel Injectors at Hypervelocity Flow Conditions**, in *52nd AIAA/SAE/ASEE Joint Propulsion Conference*, AIAA 2016-4764, AIAA, Salt Lake City, UT (Jul. 2016).
- [5] Baurle, R. A., Fuller, R. P., White, J. A., Chen, T. H., Gruber, M. R., and Nejad, A. S., **An Investigation of Advanced Fuel Injection Schemes for Scramjet Combustion**, in *36th Aerospace Sciences Meeting and Exhibit*, Reno, NV (Jan. 1998).
- [6] Ogawa, H., **Physical Insight into Fuel-Air Mixing for Upstream-Fuel-Injected Scramjets via Multi-Objective Design Optimization**, J. Propul. Power., 31(6):1505–1523 (2015).
- [7] Schetz, J. A. and Billig, F. S., **Penetration of Gaseous Jets Injected into a Supersonic Stream**, J. Spacecraft. Rockets., 3(11):1658–1665 (1966).
- [8] Mao, M., Riggins, D. W., and McClinton, C. R., **Numerical Simulation of Transverse Fuel Injection**, in *Computational Fluid Dynamics Symposium on Aeropropulsion*, NASA-CP-3078, pages 635–667, NASA, Cleveland, OH (Apr. 1990).
- [9] Portz, R. and Segal, C., **Penetration of Gaseous Jets in Supersonic Flows**, AIAA J., 44(10):2426–2429 (Oct. 2006).
- [10] Heiser, W. H. and Pratt, D. T., **Hypersonic Airbreathing Propulsion**, AIAA, Washington, DC (1994).
- [11] Public Domain Aeronautical Software (PDAS), **Properties of the U.S. Standard Atmosphere 1976**, <http://www.pdas.com/atmos.html> (Oct. 2017).
- [12] Drozda, T. G., Axdahl, E. L., and Cabell, K. F., **Pre-Test CFD for the Design and Execution of the Enhanced Injection and Mixing Project at NASA Langley Research Center**, in *JANNAF 46th CS / 34th APS / 34th EPSS / 28th PSHS Joint Subcommittee Meeting*, Albuquerque, NM (Dec. 2014).
- [13] Brown, G. L. and Roshko, A., **On Density Effects and Large Structure in Turbulent Mixing Layers**, J. Fluid Mech., 64:775–816 (1974).
- [14] Bogdanoff, D. W., **Compressibility Effects in Turbulent Shear Layers**, AIAA J., 21(6):926–927 (1983).

- [15] Papamoschou, D. and Roshko, A., ***The Compressible Turbulent Shear Layer: An Experimental Study***, J. Fluid Mech., 197:453–477 (1988).
- [16] Riggins, D. W., McClinton, C. R., and Vitt, P. H., ***Thrust Losses in Hypersonic Engines Part 1: Methodology***, J. Propul. Power., 13(2):281–287 (1997).
- [17] ***Scramjet Propulsion Testing Recommended Practices and Guidelines***, Chemical Propulsion Information Agency, 2 edn. (Mar. 2005).
- [18] VULCAN-CFD, <http://vulcan-cfd.larc.nasa.gov/> (Dec. 2017).
- [19] van Leer, B., ***Towards the Ultimate Conservative Difference Scheme. V: A Second-Order Sequel to Godunov's Method***, J. Comput. Phys., 32(1):101–136 (Jul. 1979).
- [20] Edwards, J. R., ***A Low-Diffusion Flux-Splitting Scheme for Navier-Stokes Calculations***, Comput. Fluids., 26(6):635–659 (Jul. 1997).
- [21] McBride, B. J., Gordon, S., and Reno, M. A., ***Thermodynamic Data for Fifty Reference Elements***, NASA Technical Paper 3287/REV1, NASA, Cleveland, OH (Feb. 2001).
- [22] Pulliam, T. H. and Chaussee, D. S., ***A Diagonal Form of an Implicit Approximate-Factorization Algorithm***, J. Comput. Phys., 39(2):347–363 (Feb. 1981).
- [23] Menter, F. R., ***Two-Equation Eddy-Viscosity Turbulence Models for Engineering Applications***, AIAA J., 32(8):1598–1605 (Aug. 1994).
- [24] Wilcox, D. C., ***Turbulence Modeling for CFD***, DCW Industries, Inc., La Cañada, CA (2000).
- [25] Roache, P. J., ***Verification and Validation in Computational Science and Engineering***, Hermosa Publishers (1998).

APPENDICES

A. THRUST POTENTIALS

The current approach to computing the thrust potential is illustrated in Fig. 24. The thrust potential at every streamwise location, i' , for the current flowpath is computed by expanding the local one-dimensional

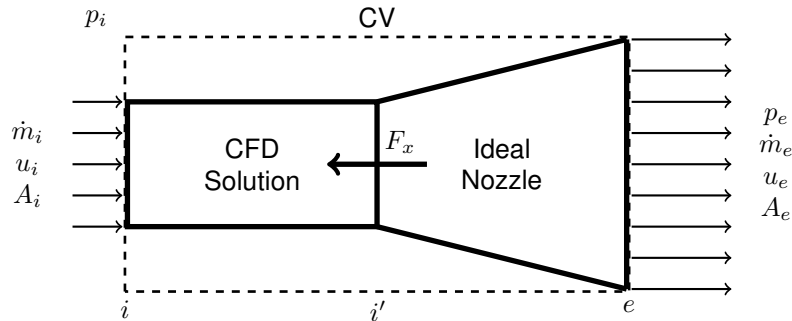


Figure 24. Illustration of the model flowpath used to compute the thrust potential in the current work.

quantities at this location through an ideal (isentropic) thrust nozzle. Conservation of momentum is then applied across the entire notional flowpath over the control volume CV and a net thrust force, F_x , is obtained:

$$F_x = p_e A_e + \dot{m}_e u_e - p_i A_i - \dot{m}_i u_i - p_i (A_e - A_i), \quad (11)$$

where the last term accounts for the force of the pressure, p_i on the external surface of the flowpath. The net thrust force is termed the thrust potential and denoted as TP because the resulting thrust is the maximum achievable. In real life, viscous and heat losses, in addition to further mixing and reaction losses of the unmixed fuel and air at i' in the nozzle, would reduce the net thrust force from this *potential* value. Equation 11 can be rearranged to resemble Eq. 3:

$$F_x = \dot{m}_e u_e + (p_e - p_i) A_e - \dot{m}_i u_i. \quad (12)$$

Because, in the current work, the inflow state is the same for all cases, the last term in the above equation is absorbed into the net thrust force on the left-hand side. Furthermore, the ideal nozzle expands the local flow to the inflow value of the static pressure. This way, the second term in Eq. 12 becomes identically zero. It should be noted that this approach to computing the thrust potential is slightly different from that used by others where the stream thrust is used instead of the net thrust. The stream thrust formulation uses the control volume that is internal to the flowpath and hence does not account for the force of the pressure on the external surface of the flowpath (i.e., last term in Eq. 11). If this term is excluded, the *stream* thrust potential equation (recast in a form similar to Eq. 12) is:

$$F_x = \dot{m}_e u_e + (p_e - p_i) A_e + p_i A_e - \dot{m}_i u_i - p_i A_i \quad (13)$$

Under the pressure-matched ideal expansion conditions, the second term in the above equation once again becomes identically zero and the last two terms can now be absorbed with the left-hand side. The third term, $p_i A_e$, would need to be computed and would serve to increase the value of the potential thrust. The increase in the value of the potential thrust computed from the stream thrust, as compared to that of Eq. 12, makes sense because accounting for the net pressure force on the external surface of the flowpath in Eq. 11 effectively amounts to accounting for some representative pressure drag, which would reduce the net thrust. With the caveats discussed above, either Eq. 12 or 13 can be used to effectively obtain the potential thrust of the flowpath, which can be used for comparative studies of performance. In the current work, Eq. 12 is adopted for this purpose.

B. DERIVATION OF THE ONE-DIMENSIONAL CORRECTIONS

The mass-flux-weighted one-dimensional (1D) value for a generic quantity, ϕ , is obtained by integrating its mass-flux weighted values on a cross-stream plane:

$$\bar{\phi} = \frac{\int^A \phi \rho u dA}{\int^A \rho u dA}, \quad (14)$$

where ρ , u , and A are the static density, streamwise velocity, and cross-stream area, respectively, and the overbar denotes the 1D value. This 1D value depends on both the extent of the area over which the integration is performed and the local values of the mass flux. The areas over which the 1D calculations are performed are different for the open flat plate and the ducted cases because their computational domains have different heights. To enable comparisons between these cases a correction to one of them is required. In the current work, the 1D corrections are applied to the open plate cases because the ducted cases have the smaller area and the 1D values carry more meaning for the ducted configuration. The problem statement is illustrated in Fig. 25. Denoting the area for which the 1D property is obtained as A_1 , Eq. 14 becomes:

$$\bar{\phi} = \frac{\int^{A_1} \phi \rho u dA + \int^{A-A_1} \phi \rho u dA}{\int^A \rho u dA} \approx \frac{\int^{A_1} \phi \rho u dA + \phi_\infty (\dot{m} - \dot{m}_1)}{\dot{m}}, \quad (15)$$

$$\bar{\phi}_1 = \frac{\int^{A_1} \phi \rho u dA}{\int^{A_1} \rho u dA} \approx \bar{\phi} \frac{\dot{m}}{\dot{m}_1} - \phi_\infty \frac{\dot{m} - \dot{m}_1}{\dot{m}_1}. \quad (16)$$
$$\dot{m}_1 \approx \dot{m} - m_\infty''(A - A_1), \quad (17)$$
$$\dot{m}_1 \approx \dot{m} - \dot{m}_\infty \frac{A - A_1}{A}, \quad (18)$$
$$\dot{m}_1 \approx \dot{m} \frac{A_1}{A}. \quad (19)$$
$$\bar{\phi}_1 \approx \bar{\phi} \frac{A}{A_1} - \phi_\infty \frac{A - A_1}{A_1}. \quad (20)$$


This last expression represents the relationship between the 1D quantity obtained over area A_1 and that computed for the larger area, A , with the assumption that the flow remains largely undisturbed over the area $A - A_1$. In the current work, A_1 is either the duct area or the IFA.